Reliable fault-ride through and protection of converter-dominated power systems under unbalanced conditions

Final Project Report

S-95

Power Systems Engineering Research Center
Empowering Minds to Engineer
the Future Electric Energy System

Reliable fault-ride through and protection of converter-dominated power systems under unbalanced conditions

Final Project Report

Project Team
Dominic Groß, Project Leader
University of Wisconsin-Madison

Maryam Saeedifard
Georgia Institute of Technology

Graduate Students
Prajwal Bhagwat
University of Wisconsin-Madison

Zexian Zheng
Georgia Institute of Technology

PSERC Publication 23-04

November 2023

For information about this project, contact:

Dominic Groß
University of Wisconsin-Madison
Department of Electrical and Computer Engineering
1415 Engineering Dr.
Madison, WI 53706
Phone: (608) 263-3106
Email: dominic.gross@wisc.edu

Power Systems Engineering Research Center

The Power Systems Engineering Research Center (PSERC) is a multi-university Center conducting research on challenges facing the electric power industry and educating the next generation of power engineers. More information about PSERC can be found at the Center's website: http://www.pserc.wisc.edu.

For additional information, contact:

Power Systems Engineering Research Center
Arizona State University
527 Engineering Research Center
Tempe, Arizona 85287-5706
Phone: 480-965-1643
Fax: 480-727-2052

Notice Concerning Copyright Material

Acknowledgments

This is the final report for the Power Systems Engineering Research Center (PSERC) research project titled “Reliable fault-ride through and protection of converter-dominated power systems under unbalanced conditions” (project S-95).

The authors wish to thank the industry advsiors: David Till (NERC), Hongtao Ma (NERC), Ben Kroposki (NREL), Kumaraguru Prabakar (NREL), Hung-Ming Chou (Dominion Energy), Aditya Jayam Prabhakar (MISO), Akshay Korad (MISO), Evangelos Farantatos (EPRI), Deepak Ramasubramanian (EPRI), Wenzong Wang (EPRI), Aboutaleb Haddadi (EPRI), Thibault Prevost (RTE), Carmen Cardozo (RTE), Harvey Scribner (SPP).

Executive Summary

At the heart of the transition towards a more sustainable electric power system is a paradigm shift from conventional bulk generation using synchronous machines to decentralized renewable generation integrated through power electronic converters. Control strategies for grid-connected power converters can be broadly categorized into (i) grid-following strategies that may provide grid-supporting services but require other devices to form a stable ac voltage waveform, and (ii) grid-forming strategies that impose a stable ac voltage waveform at their point of connection and are commonly envisioned to replace synchronous machines as the cornerstone of tomorrow's power system. Due to their comparatively low current limits, power converters cannot emulate the fault response of synchronous machines and the resulting fault-response strongly depends on the converter control and protection.

In this context, this research focuses on control and protection of grid-forming converters under unbalanced faults and load(s), the interaction of grid-forming converters with system protection, and distributed cold-start methods for unbalanced distribution feeders.

Notably, state-of-the-art grid-forming control provides a balanced voltage reference (i.e., angle and magnitude) to the converters' inner voltage and current control. However, under unbalanced conditions (i.e., faults or loading), the inner control loops cannot track a balanced voltage reference at the converter terminal. Moreover, for common converter topologies such as two-level voltage source converters, the current limits need to be enforced for every phase. However, state-of-the-art controls do not have this capability. To address this challenge and fully leverage the degrees of freedom of grid-forming converters, this project developed a generalized three-phase grid-forming control. The developed control combines a signal processing algorithm that extracts phasors for every phase signal of a three-phase converter with a generalized control architecture that applies state-of-the-art grid-forming controls and current limiting separately to every phase. In addition, a phase-balancing feedback is developed to synchronize the controls of every phase and adjust tradeoffs between voltage unbalance, power unbalance as well as the sharing of unbalanced load by multiple converters.

A steady-state analysis reveals how the tuning parameters of the generalized three-phase grid-forming control can be used to adjust tradeoffs between voltage unbalance and power unbalance, as well as how much load unbalance is picked up a grid-forming converter. Moreover, we will briefly review results of an analytical small-signal stability analysis that highlights that small-signal frequency stability of the generalized three-phase droop control can be ensured under mild conditions that are comparable to those required to ensure small-signal stability of standard (positive sequence) grid-forming controls.

This approach also allows us to apply standard current limiting methods to each phase. We first investigate applying two widely used methods (i.e., reference current saturation and threshold virtual impedance) to every phase of a grid-forming converter. Notably, both approaches inherit well-known advantages and disadvantages from their balanced implementation. In particular, reference current saturation limits the current exactly and is easy to tune but suffers from a loss of synchronism for prolonged faults (i.e., short critical clearing time). In contrast, threshold virtual impedance largely avoids the loss of synchronism (i.e., long critical clearing time) but is ineffective if the difference between the converter phase angle and phase angle the point of interconnection is

large (i.e., after clearing a fault or tripping a line). To address this challenge, we developed a hybrid threshold virtual impedance method that can effectively limit the converter current under large phase angle jumps.

Finally, we developed an initial method for distributed cold-start methods for unbalanced distribution feeders that do not require centralized coordination and leverage the capabilities of distribution connected grid-forming converters and advanced load relays. Instead of energizing an entire distribution feeder at once, this approach relies on autonomously sequencing the energization of loads at a more granular level during a cold-start process initiated by grid-forming converters.

The effectiveness of the control algorithms developed in this project and study the interactions of grid-forming converters with the system protection, we developed two benchmark systems. The first benchmark system models a segment of a system consisting of a medium voltage feeder and a high voltage double circuit transmission line and is used to study transmission faults and interactions of the converter control and protection with distance relays. The second benchmark model is based on the IEEE 13-bus feeder and is used to study (i) the impact of loads (i.e., unbalanced loads, induction machine startup) on grid-forming converters and current limiting, (ii) interactions of grid-forming converters with protection (i.e., inverse time relays), and (iii) cold-start of unbalanced distribution systems.

Project Publications:

[1] P. Bhagwat, D. Groß, “Three-phase grid-forming droop control for unbalanced systems and fault ride through,” IEEE Power & Energy Society General Meeting, 2023

[2] Z. Zeng, P. Bhagwat, M. Saeedifard, D. Groß, “Hybrid Threshold Virtual Impedance for Fault Current Limiting in Grid-Forming Converters,” IEEE Energy Conversion Congress & Exposition, 2023

[3] S. Nudehi, D. Groß, “Grid-forming control of three-phase and single-phase converters across unbalanced transmission and distribution systems”, IEEE Transactions on Power Systems, to appear

[4] Z. Zeng, P. Bhagwat, M. Saeedifard, D. Groß, “Black Start Operation of Grid-Forming Converters Based on Generalized Three-Phase Droop Control Under Unbalanced Conditions,” Submitted to CIGRE Session, Paris, 2024.

Student Theses:

[1] P. Bhagwat, Three-phase grid-forming droop control for unbalanced systems and fault ride through, MS thesis, 2023

[2] P. Bhagwat, Constrained grid-forming control, PhD, in progress

[3] Z. Zeng, Control of Multi-terminal HVDC Grids for Integration of Offshore Wind Farms, PhD, in progress

Table of Contents

List of Figures

List of Tables

1. Introduction

1.1 Background

At the heart of the transition towards a more sustainable electric power system, there is a paradigm shift from conventional bulk generation using synchronous machines to decentralized renewable generation interfaced by power electronic converters. Several countries and US states, such as Minnesota and California, aim to complete the transition to a 100% renewable system by 2040 to 2050, and large-scale converter-dominated power systems are quickly becoming a reality. During the first half of 2020, the share of instantaneous wind and PV generation in South Australia peaked at 85% (median 55%), while it reached a maximum of 58% (median of 38%) in the Texas Interconnection. In contrast to synchronous machines, most renewable generation deployed today does not contribute to stabilizing power system, does not provide reliable fault-ride through, and can trigger adverse interactions with protection systems. These shortcomings jeopardize system reliability and resilience and, together with a sharp increase in severe weather-related equipment outages [3], have already resulted in large-scale service interruptions [4], system outages [5], and separation events [6]. Control strategies for grid-connected power converters can be broadly categorized into (i) grid-following strategies that may provide grid-supporting services but require other devices to form a stable ac voltage waveform to lock on to and are highly sensitive to disturbances [4,5], and (ii) grid-forming strategies that impose a stable ac voltage waveform at their point of connection and are envisioned to replace synchronous machines as the cornerstone of tomorrow's power system [7]. However, due to their comparatively low current limits, power converters cannot emulate the fault response of synchronous machines. Consequently, the fault-response of a converter-dominated power system vastly differs from the response expected by today's system-level protection [8, 9] and strongly depends on the converter control and protection. Therefore, a comprehensive approach that accounts for converter control, converter protection, and system-level protection is required to ensure reliability of tomorrow's power system. While most faults are unbalanced [10], state-of-the-art grid-forming control strategies are designed assuming a balanced grid and have significant architectural shortcomings that cannot be overcome by minor modifications. Therefore, this proposal aims to develop a framework that explicitly accounts for unbalanced conditions and faults, converter protection (i.e., current limiting), and system-level protection requirements in the grid-forming control design to provide a reliable and resilient foundation for tomorrow's converter-dominated power systems.

While large-scale converter-dominated bulk power systems have been a theoretical concept until a few years ago, they are rapidly becoming a reality. One of the critical obstacles for transitioning to a sustainable zero-carbon power system is reliable and resilient control of power converters. Typically, control strategies for grid-connected power converters can be broadly categorized into (i) grid-following (GFL) controls that assume a stable AC voltage (i.e., magnitude and frequency) and (ii) grid-forming (GFM) strategies that form a stable AC voltage (i.e., magnitude and frequency) at the converter terminal [11]. As a consequence of relying on a stable AC voltage, GFL control

may fail due to voltage disturbances [4] or if insufficient GFM units (i.e., synchronous generators or GFM converters) are online to ensure frequency stability.

In contrast, GFM power converters can form a stable grid and are envisioned to be the cornerstone of future power systems. While originally developed in the context of microgrids, grid-forming power converters are commonly envisioned to as cornerstone of future bulk power systems [12].

At the same time, several systems around the world are already facing challenges due to massive renewable integration that can be traced back to a lack of reliable fault-ride through [4,5] and adverse interactions of power converters and protection algorithms designed for the legacy system [6]. To overcome these issues, we envision a future power system with 100% converter-based renewable generation that consists of a mix of grid-following and grid-forming power converters. In such a system, grid-forming units need to ensure that the system rides through any fault and that frequency remains well-defined so that legacy grid-following units can synchronize to a converter-dominated system and respond to changes in frequency.

Recent works have shown that, from a frequency stability perspective, state-of-the-art grid-forming converter control has the potential to replace synchronous machines. However, power converters cannot replicate the fault response of machines, and new paradigms are required to ensure reliable operation in the presence of faults. To this end, this report aims to

- extend the design of grid-forming controls to unbalanced conditions to unlock its flexibility for unbalanced operation both during faults and on longer time scales,
- design current limiting strategies that enable reliable and predictable fault-ride through of grid-forming converters and retain their positive impact on system-level stability when feasible,
- provide a path towards closing the gap between converter control and protection systems.

1.2 Literature review

State-of-the-art grid-forming (GFM) control generates a balanced terminal voltage reference [13, 14] (i.e., phase angle and magnitude) that is tracked by the converters' inner cascaded current and voltage control.

Key advantages of GFM control include its fast response to contingencies [7] and potential for fast fault current injection. However, due to their comparatively low current limits, they cannot emulate the fault response of synchronous machine [15]. In contrast, synchronous generators provide a fault response that is constrained solely by the electromechanical limits of synchronous generators [16, 17]. Consequently, the fault-response of a converter-dominated power system may vastly differ from the response expected by today's system protection [9]. For example, GFL converters leverage constant current injection to ride through faults [18]. However, the (self-synchronizing) voltage source characteristics of GFM converters are not amenable to this approach. Crucially,

common GFM controls that generate a balanced voltage reference cannot fully control the converter current injection or terminal voltage under unbalanced output current. Therefore, common grid-forming controls cannot actively mitigate imbalances on the system, even if unbalanced setpoints are provided by secondary or tertiary controls. Similarly, common strategies for current limiting in GFM voltage source converters (VSCs) such as limiting the reference of the inner current controller [15], threshold virtual impedance [15, 19, 20], and projected droop control [21] assume a balanced system and balanced faults. At the same time, the vast majority of faults in high voltage systems are unbalanced [10].

Moreover, distribution systems typically exhibit significant unbalance that (i) is typically not accounted for in the literature on design and analysis of GFM controls, and (ii) can be mitigated by deploying GFM converters in distribution systems. The few works that consider GFM control under unbalanced conditions [22, 23] and faults [23] typically leverage symmetrical components, e.g., implementing separate GFM controls for positive and negative sequence. This approach is motivated by prevailing analysis methods for unbalanced systems using symmetrical components and can effectively control the VSC terminal voltage under unbalanced conditions. However, the relationship between the converter phase currents and symmetrical components is highly nonlinear [23] and limiting the phase currents through control of symmetrical components results in challenging control design and analysis problems. A noteworthy exception is the work in [24] that combines dispatchable virtual oscillator control [25] with proportional resonant inner control loops and threshold virtual impedance current limiting to directly control the converter voltage and current in $\alpha\beta$-frame to enable unbalanced fault-ride through capabilities. While this approach results in a low complexity control architecture, the performance of proportional resonant controls is often limited, and the method does not allow to directly impose the phase current limits typically encountered in three-phase voltage source converters through the control in $\alpha\beta$-frame.

Finally, the vast majority of studies on fault ride through of GFM converters does not model the protection system and hence does not provide an understanding of interactions between GFM converter controls, converter protection, and system protection. A notable exception is the work [26] that studied various GFM controls and current limiting schemes and concluded that virtual impedance current limiting results in reliable operation of distance protection.

Overall, we conclude that there is a need for GFM control architecture that enable GFM converters to fully control their terminal voltage under severely unbalanced conditions and faults, limit the converter phase currents, and actively contribute to mitigating phase unbalance through sharing load unbalance.

While the integration of distributed energy resources into distribution systems challenges conventional protection paradigms, it also offers increased controllability of distribution feeders. In this context, a crucial feature of GFM control, applied to power converters with sufficient overcurrent capability, is the ability to cold-start a system. By leveraging GFM converters, recent developments highlight the bottom-up restoration of a complete blackout system with no energization from the upstream network [27]. Opportunities for advanced protection and cold-start mechanisms tailored to the cold-start capabilities of grid-forming have only recently been investigated in [28] without

traditional communication or overlaid control. However, these results do not consider unbalanced loading typically encountered in distribution systems and also do not fully account for the significant impact of current limiting schemes in GFM controls. The cold-start capability of GFM converters in unbalanced systems is explored in [29], leveraging symmetrical components with current limiters to limit the currents in the *abc* frame. Nonetheless, this method requires the calculation of the Root Mean Square (RMS) value for each phase current, a process introducing delays and potentially leading to significant overcurrent occurrence for durations exceeding one cycle.

1.3 Outline

This report is structured as follows. Chapter 2 introduces the problem setup, converter model used throughout this report, and reviews common representations for unbalanced signals. Next, Chapter 3 reviews standard GFM control architectures and presents the generalized three-phase GFM control architecture developed in this project. Chapter 4 extends two common current limiting approaches (i.e., reference current limiting and threshold virtual impedance) to facilitate limiting of phase currents and presents a hybrid threshold virtual impedance method that improves upon the performance of threshold virtual impedance methods. A theoretical analysis of the properties of the generalized three-phase GFM control dynamics and its steady-state response is presented in Chapter 5. Chapter 6 briefly introduces a conceptual solution for distributed cold-start methods for unbalanced distribution feeders that does not require centralized coordination. Case studies using benchmark systems with explicit models of system-level overcurrent protection are presented in Chapter 7 and Chapter 8. Finally, Chapter 9 provides conclusions and directions for future work.

2. Preliminaries and Problem Setup

The ability of a grid-connected power converter to control its terminal voltage and/or current injection under unbalanced load or unbalanced faults crucially hinges on both its controls and internal converter topology. In this section, we first review different representations of converter currents and voltages that will inform our control design. Moreover, we briefly discuss the model of a three-phase voltage source converter used throughout this report.

2.1 Coordinate frames

The three-phase ac signals generated by a three-phase power converters are often represented in two forms. First, for the purpose of control, signals are commonly represented through their instantaneous value at a given time. In other words, if $x(t) \in \mathbb{R}$ is real-valued signal at time $t \in \mathbb{R}$ and may capture a phase current or voltage. In addition, if $x(t)$ is sinusoidal with constant time period / frequency and magnitude $\|x(t)\| := \hat{x}$ where $\|\cdot\|$ is euclidean norm, then considering the total time period as 2πrad, a phase angle $\theta \in [0, 2\pi]$rad and magnitude $\hat{x}$ can be associated with every time t. This results in the well-known phasor representation of a sinusoidal signal, i.e., $\hat{x}e^{j\theta} = \hat{x}(\cos\theta + j\sin\theta)$, where $j = \sqrt{-1}$.

2.1.1 Synchronous reference frame

When the GFM converter is operating under balanced conditions, it is customary to apply the so-called $dq0$ transformation. This transformation is composed of Clarke and Park transformation. Let $x_p(t) := \hat{x}_p \cos(\omega_p t + \theta_p) \in \mathbb{R}$ be a time domain ac signal of phase $p \in \mathscr{P} := \{a, b, c\}$ with amplitude $\hat{x}_p \in \mathbb{R}$ at time $t \in \mathbb{R}$. Assuming the signal has a constant frequency $\omega = \omega_p \in \mathbb{R}$ for every phase $p \in \mathscr{P}$, then the sinusoidal three-phase signal $(x_a(t), x_b(t), x_c(t)) \in \mathbb{R}^3$ can be transformed into a constant signal using the $dq0$ transformation

$$\begin{bmatrix} x_d(t) \\ x_q(t) \\ x_0(t) \end{bmatrix} = \sqrt{\frac{2}{3}} \begin{bmatrix} \cos(\omega t) & \cos\left(\omega t - \frac{2\pi}{3}\right) & \cos\left(\omega t + \frac{2\pi}{3}\right) \\ -\sin(\omega t) & -\sin\left(\omega t - \frac{2\pi}{3}\right) & -\sin\left(\omega t + \frac{2\pi}{3}\right) \\ \frac{\sqrt{2}}{2} & \frac{\sqrt{2}}{2} & \frac{\sqrt{2}}{2} \end{bmatrix} \begin{bmatrix} x_a(t) \\ x_b(t) \\ x_c(t) \end{bmatrix}. \tag{2.1}$$

If the voltage or current are balanced, then $x_0(t) \in \mathbb{R}$ is zero and $x_d(t) \in \mathbb{R}$, $x_q(t) \in \mathbb{R}$ are constant. However, if the system is unbalanced, $x_0(t) \in \mathbb{R}$ is zero and $x_d(t) \in \mathbb{R}$, $x_q(t) \in \mathbb{R}$, and $x_0(t) \in \mathbb{R}$ are not necessarily constant and will, generally, contain a double frequency component. Notably, in studies of grid-connected converters the zero sequence components $x_0(t) \in \mathbb{R}$ of voltage and/or current are typically neglected because no zero sequence current can flow in three-wire systems and grid-forming converters are controlled not to apply any zero sequence voltage to the system.

2.1.2 Symmetrical components

Unlike dq-transformation applied to instantaneous signals, the symmetrical components make use of the phasor $\hat{x}_p(\cos\theta_p + j\sin\theta_p) \coloneqq \mathbf{x}_p \in \mathbb{C}$ where $p \in \mathscr{P}$. Symmetrical components of a three-phase system can be represented as

$$\begin{bmatrix} \mathbf{x}^+ \\ \mathbf{x}^- \\ \mathbf{x}^0 \end{bmatrix} = \frac{1}{3} \begin{bmatrix} 1 & 1 & 1 \\ 1 & \alpha & \alpha^2 \\ 1 & \alpha^2 & \alpha \end{bmatrix} \begin{bmatrix} \mathbf{x}_a \\ \mathbf{x}_b \\ \mathbf{x}_c \end{bmatrix}. \tag{2.2}$$

Here, $\alpha = e^{j\frac{2\pi}{3}}$, and $\mathbf{x}^+ \in \mathbb{C}$, $\mathbf{x}^- \in \mathbb{C}$, and $\mathbf{x}^0 \in \mathbb{C}$ denote the positive, negative and zero sequence components of the three-phase signal modeled by the phasors $\mathbf{x}_a \in \mathbb{C}$, $\mathbf{x}_b \in \mathbb{C}$, and $\mathbf{x}_c \in \mathbb{C}$. Assuming a balanced three-phase system, the negative and zero sequence components are zero. However, in contrast to the $dq0$ transformation, the representation of an unbalanced signal through symmetrical components still remains insightful for unbalanced signals and is commonly used in fault analysis and for protection design and studies. Nonetheless, two challenges are associated with the use of symmetrical components in the context of grid-forming control. First, the transformation (2.2) crucially hinges on modeling the phase currents or voltages as phasors that have to be estimated from their instantaneous values. Second, the relationship between phase currents and their representation in symmetrical components is highly nonlinear and makes the problem of limiting converter phase currents challenging from both practical and theoretical perspectives.

2.1.3 Hilbert transform

As seen in the previous subsections, a balanced three-phase system is easily represented by instantaneous values of current and voltage. However, for analysis of unbalanced systems the representation in symmetrical components is the prefered tool but cannot be applied using instantaneous values. Thus, obtaining a phasor representation of instantaneous sinusoidal signals is a key problem. A common approach in power electronics to resolve this challenge is the so-called Hilbert transform that estimates the quadrature component of every phase signal by applying a time shift that corresponds to a 90° phase shift.

To formalize this approach in the context of GFM control, assume that $\omega_p \in \mathbb{R}$ denotes a reference frequency for each phase $p \in \mathscr{P}$ that is provided by a GFM control. Then, for all $p \in \mathscr{P}$ and any ac signal $x_p(t)$, we estimate the quadrature component $x_p^\perp(t) \in \mathbb{R}$ of $x_p(t) \in \mathbb{R}$ as

$$x_p^\perp(t) \coloneqq x_p(t - \tfrac{1}{4}\tfrac{1}{\omega_p(t)}). \tag{2.3}$$

In other words, under the assumption that $x_p(t)$ is a sinusoidal signal with slowly changing frequency $\omega_p(t)$, the time shift in (2.3) approximates a 90° phase shift. Notably, the Hilbert transform can be interpreted as representing $\alpha\beta$ components of an ac signal (i.e., $(x_{p,\alpha}, x_{p,\beta}) = (x_p, x_p^\perp)$). Let $R(\cdot)$ denote the 2D rotation matrix (Park transformation). Then, any ac signal $x_p(t) \in \mathbb{R}$ for any

phase $p \in \mathscr{P}$ can be represented in a dq frame with reference angle $\theta_p(t) \in \mathbb{S}$ as

$$x_{p,dq}(t) \coloneqq \begin{bmatrix} x_{p,d}(t) \\ x_{p,q}(t) \end{bmatrix} \coloneqq R(\theta_p(t)) \begin{bmatrix} x_p(t) \\ x_p^{\perp}(t) \end{bmatrix}. \tag{2.4}$$

where $\frac{\mathrm{d}}{\mathrm{d}t}\theta_p(t) = \omega_p(t)$ is an arbitrary frequency. Moreover, for any ac signal $x_p(t) \in \mathbb{R}$ we can construct a corresponding phasor $\mathbf{x}_p(t) \in \mathbb{C}$, i.e.,

$$\mathbf{x}_p(t) \coloneqq x_{p,d}(t) + j x_{p,q}(t). \tag{2.5}$$

2.2 Power converter model

The most prevalent grid-connected power converter topology is the so-called two-level three-phase dc/ac voltage source converter (VSC) shown in Figure 2.1. For brevity of the presentation, we will focus on this topology throughout this report. Moreover, for analytical studies and control design we will consider an averaged converter model (i.e., neglect switches and modulation schemes) and assume that the converter dc terminal is connected to a constant dc voltage. When necessary to ensure validity of the results, our case studies will include a simulation of the switches and modulation strategy. We emphasize that, while the assumption of a constant dc voltage is commonly made in the design and analysis of GFM controls, it is only fully justified for IBR resources with significant energy storage (e.g., battery energy storage systems) and needs to be revisited for common renewable sources (e.g., PV and wind turbines) in future studies.

Additionally, throughout this report we assume that the midpoint of the dc source is grounded (midpoint grounding scheme) as shown in Figure 2.1. This arrangement can be understood as an equivalent model of a dc/ac voltage source converter with dc-link capacitor and grounding of a midpoint that is created using resistors or capacitors between the positive and negative dc pole. We note that several other grounding schemes (e.g., floating dc side) are possible. For the purpose of this report we chose to focus on the setup as shown in Figure 2.1 that allows zero sequence current flow. If, e.g., a floating dc side is used, zero sequence current cannot flow and the control degrees of freedom of the converter are reduced. In this case, the controls have to be adapted to account for this fact. For instance, for the generalized three-phase GFM control presented in Section 3.4, voltages and currents have to be transformed to a coordinate frame that eliminates zero sequence components (e.g., $\alpha\beta$ coordinates) and separate GFM controls can be used for the remaining two components (e.g., α and β) instead of separate GFM controls for every phase.

Finally, VSCs are interconnected to the grid via an LCL filter to remove the switching ripple introduced by the modulation scheme. The filter capacitors are typically either configured in Δ or $\curlyvee$ configuration. For two-level VSCs with grounded neutral point as shown in Figure 2.1, the filter capacitors are commonly $\curlyvee$ configured and the dc neutral point is connected to the ground of the $\curlyvee$ configured filter capacitors. This closes the path for the zero current ot flow. We have chosen this arrangement because it allows the VSC to fully control each phase voltage and/or current and showcase the features of the controls developed in this project. In contrast, a Δ configured filter is commonly used with a floating DC bus and hence removes the zero sequence current path. In this

case, the controls developed in this project can be implemented in, e.g., $\alpha\beta$ coordinates as outlined above.

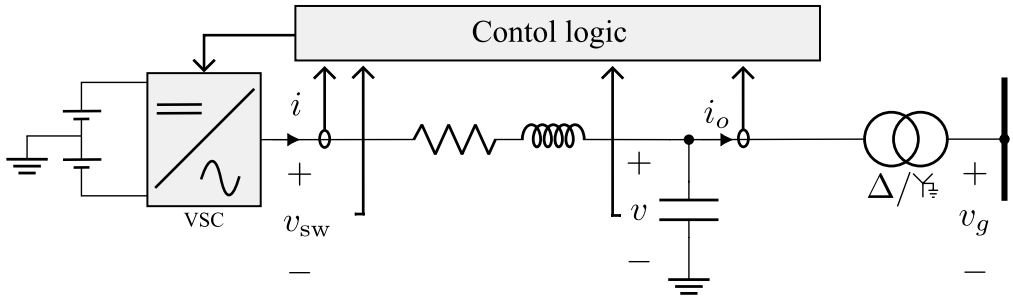

Figure 2.1: GFM converter consisting of a 2-level VSC with grounded midpoint. Moreover, we assume that the output filter is Y_N configured and that a ΔY_N transformer is used to connect the VSC to the grid.

Finally, we assume that converter is connected to the grid through a ΔY_N transformer where Δ is on the primary side and the Y_N is on the secondary. The advantage of this arrangement is to provide solid grounding of the grid that provides a pathway for zero sequence fault current. We emphasize that, in addition to the dc grounding and filter arrangement, different transformer configurations may also require implementing the controls presented in Chapter 3 and Chapter 4 on different coordinate frames than those used in Chapter 3 and Chapter 4.

3. Grid-forming control

This chapter first reviews our basic control objectives for GFM converters and reviews existing controls from the literature in more detail. Subsequently, we present the generalized three-phase GFM controls developed in this project.

3.1 Control objectives and architectures

The key motivation for common GFM control designs is to enable VSCs to provide reliable grid-support functions that allow GFM resources to largely replace synchronous generators in bulk power systems. To this end, a GFM VSC should meet the following key control objectives.

1. Impose an ac voltage waveform with well-defined frequency and amplitude to the grid and self-synchronize with other GFM resources and synchronous generators through the power network.

2. During nominal steady-state operation, the converter needs to be controlled to the nominal operating point (i.e., voltage, frequency, and power) periodically prescribed by a system-level controller.

3. The converter should autonomously respond to variations in load or generation and contingencies to support the system through, e.g., primary control functions, and contribute to stabilizing the system frequency and voltage.

4. The converter control needs to ensure operation within the converter hardware limits (e.g., rated current of the semiconductor switches).

Notably, these high-level objectives align with the high-level functions of synchronous generators except for the response to faults. In particular, synchronous generators have significant overcurrent capabilities (i.e., up to 6 p.u. for a short period of time) while the semiconductor switches of power electronic converters are typically only sized to withstand currents of approximately 1.4 p.u. for one or two cycles and are typically limited to approximately 1.2 p.u. otherwise. We emphasize that, by oversizing the converter relative to its power source, the current limits can be increased. However, this comes at a significantly increased cost and is usually avoided for economic reasons. Hence, a key question is how to limit the converter output current and while providing GFM functions and ensuring availability of sufficient fault current to reliably trip protective relays.

The standard cascaded dual-loop control structure for GFM controlled grid-connected voltage source converters is shown in Figure 3.1. Specifically, the aforementioned control objectives are commonly met through a hierarchical control structure consisting of an outer GFM control that provides references for the dynamic response at the converter terminal to inner cascaded controls that

stabilize and control the converter. In this context, the converter overcurrent protection is typically either implemented at the switch level (not shown in Figure 3.1) through, e.g., blocking of switches if the current across the switch would exceed its limits, or at the level of the current controller as shown in Figure 3.1.

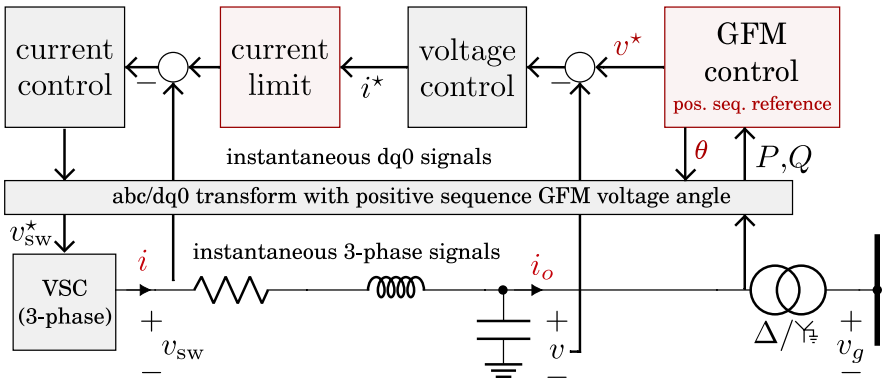

Figure 3.1: Standard dual-loop GFM control with inner controls tracking a positive sequence voltage reference provided by an outer GFM control (e.g., droop control [1], VSM [2]).

3.2 Positive sequence droop control

The most prevalent grid-forming control strategy is droop control and computes a balanced positive sequence reference voltage with voltage magnitude $V^{\text{gfm}} \in \mathbb{R}$ and angle $\theta^{\text{gfm}} \in \mathbb{S}$ that is tracked by underlying proportional-integral controls implemented in a dq frame with angle $\theta^{\text{gfm}} \in \mathbb{S}$ as shown in Figure 3.1.

Positive sequence droop control is realized as

$$\tfrac{\mathrm{d}}{\mathrm{d}t}\theta^{\text{gfm}} = \omega_0 + m_P(P^\star - P), \tag{3.1a}$$

$$V^{\text{gfm}} = V^\star + m_Q(Q^\star - Q), \tag{3.1b}$$

where, $\omega_0 \in \mathbb{R}_{>0}$ is the base frequency, $m_P \in \mathbb{R}_{>0}$ and $m_Q \in \mathbb{R}_{>0}$ are the active and reactive power droop coefficients. Moreover, $V^\star$, $P^\star$ and $Q^\star$ are references for the voltage, active power and reactive power, and P and Q are the measured active and reactive power.

We emphasize that, the outer GFM control can be combined with various methods for current limiting such as reference current limiting as shown in Figure 3.1 or virtual impedance current limiting [19]. This aspect will be discussed in detail in the next chapter.

Finally, we note that the inner controls are commonly implemented in a dq-frame with reference angle θ^{gfm}, i.e., the instantaneous signals $v_{sw} \in \mathbb{R}^3$, $i \in \mathbb{R}^3$, $v \in \mathbb{R}^3$ and $i_o \in \mathbb{R}^3$ for all three-phases are converted into a dq frame for the purpose of implementing the inner controls and current limiting. We emphasize that, for a balanced system, limiting the current in the dq frame to its maximum also limits the phase currents to their maximum.

While this overall approach significantly simplifies the control design in for a balanced system, it precludes leveraging all degrees of freedom of the convert during unbalanced operation. In particular, in this case, the signals in dq-frame will not correspond to constant signals even in steady state and, e.g., limiting the filter current to its maximum in dq frame can result in severe distortion in the original *abc* coordinates (see, e.g., [21, Figure 7]).

Ultimately, during severely unbalanced conditions such as faults, positive sequence droop control aims to impose a balanced voltage at its terminals. However, under the converter current limits the underlying controls may not be able to impose the balanced reference at the terminal resulting in distorted waveforms and, ultimately, a lack of reliable and resilient fault ride through capabilities.

Loosely speaking, the limitations of positive sequence droop control can be overcome by implementing the GFM control and inner controls in symmetrical components [23,30] or for every phase. This allows to leverage the degrees of freedom of the VSC. Next, we will briefly discuss implementations using symmetrical components. Then, we will present a generalized three-phase droop control that implements GFM control and inner loops for every phase.

3.3 Positive-negative sequence droop control

To illustrate the main features of positive-negative sequence droop control, we focus on an implementation similar to the positive-negative sequence synchronverter presented in [30]. We emphasize that more involved approaches exist that may result in increased performance (see, e.g., [23]). However, for brevity of the presentation we focus on positive-negative sequence droop control to highlight the main conceptual challenges of positive-negative sequence GFM control.

Positive-negative sequence droop control generates a positive and negative sequence reference voltage with angle and magnitude given by

$$\tfrac{\mathrm{d}}{\mathrm{d}t}\theta^{+} = \omega_0 + m_P^{+}(P^{+\star} - P^{+}), \tag{3.2a}$$
$$\tfrac{\mathrm{d}}{\mathrm{d}t}\theta^{-} = \omega_0 + m_P^{-}(P^{-\star} - P^{-}), \tag{3.2b}$$
$$V^{+} = V^{+\star} + m_Q^{+}(Q^{+\star} - Q^{+}), \tag{3.2c}$$
$$V^{-} = V^{-\star} + m_Q^{-}(Q^{-\star} - Q^{-}). \tag{3.2d}$$

We recall that the superscripts $(\cdot)^{+}$ and $(\cdot)^{-}$ denote the positive and negative sequence voltage phase angles, magnitudes, powers, and control gains. This control is typically implemented by first estimating the positive and negative sequence components of the converters' power injection, using (3.2) to obtain positive and negative sequence voltage references, and underlying cascaded controls for positive and negative sequence current and voltage that track the references. Alternatively, the positive and negative sequence voltages can be converted into *abc* coordinates and tracked by underlying controls (e.g., proportional resonant controls) for every phase.

A key challenge with this approach is estimation delay of the filter used to obtain the associated positive and negative components of the converter currents and voltages. Moreover, the relationship between positive and negative sequence currents and phase currents is highly nonlinear. This makes the design of current limiters and analysis of the system a challenging problem.

However, the main problem with the aforementioned approach is that it does not autonomously trade off power and voltage unbalance. In particular, assuming a balanced nominal operating point, i.e., letting $V^{-\star} = 0$, $Q^{+\star} = 0$, and $P^{-\star} = 0$, always results in $V^- = 0$ unless the current limit is active. In particular, if no current limit is active, the inner loops will perfectly track the reference $V^- = 0$ and hence $Q^+ = 0$, and $P^- = 0$, even if the converter current injection $i_o \in \mathbb{R}^3$ is unbalanced. Consequently, V^- will remain at zero and the converter will impose a balanced voltage.

An alternative solution is to directly droop on the output current. To this end, we note that the negative sequence phasors can be represented through a dq frame aligned with the phase angle of the negative sequence voltage phasor $v^- \in \mathbb{C}$. Then, the negative sequence powers are given by

$$P^- = \frac{3}{2}(v_d^- i_d^- + v_q^- i_q^-), \tag{3.3}$$
$$Q^- = \frac{3}{2}(v_q^- i_d^- - v_d^- i_q^-). \tag{3.4}$$

Moreover, the coordinate frame is typically aligned such that $v_q^- = 0$ and hence

$$P^- = \frac{3}{2}(v_d^- i_d^-), \tag{3.5}$$
$$Q^- = \frac{3}{2}(-v_d^- i_q^-). \tag{3.6}$$

Implementing the negative sequence droop equations using negative sequence current results in

$$\tfrac{\mathrm{d}}{\mathrm{d}t}\theta^- = \omega_0 + m_P^-(i^{-\star} - i_d^-), \tag{3.7a}$$
$$V^- = V^{-\star} + m_Q^-(i^{-\star} + i_q^-). \tag{3.7b}$$

While this approach may appear more intuitive from a power system point of view and avoids the problems associated with the fact that $v_d^- = 0$ during nominal operation, its interpretation may not be straightforwards. In particular, the reformulation from power to current only results in a similar

response if $v_d^- \approx 0$. However, in most scenarios, v_d^- will be small and hence the control (3.7) will trade off negative sequence voltage and current as expected (i.e., an increase in m_Q^- results in a decrease of i_q^-). However, the same is not true for negative sequence voltage and power. An example for a GFM converter feeding an unbalanced load can be found in Section 7.2.2.

3.4 Generalized three-phase droop control

Because of the challenges associated with positive-negative sequence GFM control, this project instead explored GFM controls that can control each converter phase. To this end, this project developed a generalized three-phase GFM control architecture shown in Figure 3.2 that implements the GFM control, inner controls, and current limiting separately for each phase. A phase-balancing feedback synchronizes the outer GFM control and thereby ensures a controlled trade-off between power unbalance, voltage unbalance, and also allows to control the converters' contribution to mitigating unbalance.

To be able to control the phase voltages and/or currents individually, we estimate a phasor for every phase signal using the Hilbert transform described in Section 2.1.3. This allows us to represent the signals for every phase in a separate dq-frame and implement the standard inner current and voltage controls for every phase (see Chapter 4 for details) to obtain the phase powers $P_p \in \mathbb{R}$ and $Q_p \in \mathbb{R}$. To apply the Hilbert transform, we require a reference frequency $\omega_p^{\text{gfm}} \in \mathbb{R}$ for every phase. This is obtained from the GFM control for every phase that also provides a phase angle $\theta_p^{\text{gfm}} \in \mathbb{S}$ and voltage $V_p^{\text{gfm}} \in \mathbb{R}$ for every phase $p \in \mathscr{P}$.

The inner voltage controller then tracks the voltage reference phasors for every phase by calculating corresponding current reference. The resulting current reference for every phase can then be limited individually as shown in Figure 3.2 and tracked by individual inner current controllers. Alternatively, virtual impedance current limiting can be applied to every phase instead of reference current limiting (see Chapter 4). We emphasize that, analogously to positive sequence GFM control, the gains of inner and outer loops need to be coordinated and chosen relative to the network circuit dynamics to ensure performance and stability [31, 32].

Finally, the outer GFM control combines GFM droop control for every phase with a phase balancing feedback that (i) ensures balanced reference voltages $V_p^{\text{gfm}} \in \mathbb{R}$ and phase angles $\theta_p^{\text{gfm}} \in \mathbb{S}$ if the system is balanced, and (ii) allows trading off voltage and power unbalances under unbalanced conditions and faults.

To implement the control, the Hilbert transform (2.3) is applied to the voltages $v_p(t)$ and current $i_p(t)$ for each phase p to estimate their quadrature components. Then, the average active power P_p and reactive power Q_p over one cycle can be computed using their corresponding current phasor $\mathbf{i}_p(t)$ and voltage phasor $\mathbf{v}_p(t)$ as follows

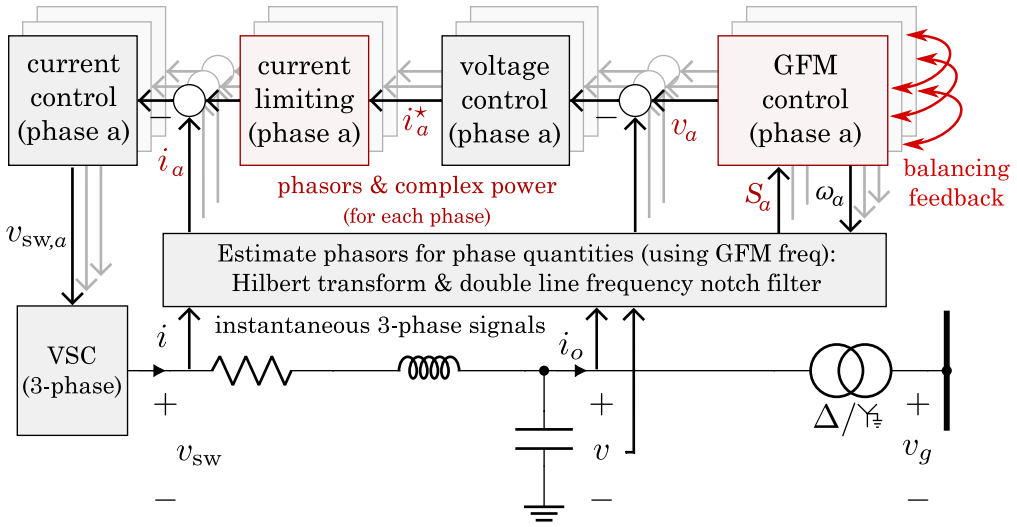

Figure 3.2: Generalized three-phase GFM control with inner control for every phase tracking a voltage reference provided by the outer GFM control (3.9) with phase balancing feedback.

$$P_p(t) := \tfrac{1}{2}\mathrm{Re}(\mathbf{v}_p\overline{\mathbf{i}_p}) = \tfrac{1}{2}\left(v_p(t)i_p(t) + v_p^\perp(t)i_p^\perp(t)\right), \tag{3.8a}$$

$$Q_p(t) := \tfrac{1}{2}\mathrm{Im}(\mathbf{v}_p\overline{\mathbf{i}_p}) = \tfrac{1}{2}\left(v_p^\perp(t)i_p(t) - v_p(t)i_p^\perp(t)\right). \tag{3.8b}$$

Because of controller sampling rate limits, the time-shift operation in (2.3) cannot be implemented to arbitrary accuracy in a digital controller. This results in a frequency component at two times the converter frequency ω_p in the measurements of P_p and Q_p. This component is removed using a notch filter with center frequency $2\omega_p$. The average phase powers P_p and Q_p are then used to compute the reference frequency $\omega_p(t)$ and voltage reference (i.e., phase angle and magnitude) for every phase through the three-phase GFM control presented in the next section. In other words, the Hilbert transform and GFM control are in a feedback interconnection, i.e., at every sampling time the reference frequency $\omega_p(t)$ for every phase is used in the Hilbert transform and compute updated phase powers $P_p(t)$ and $Q_p(t)$ obtained from the Hilbert transform are used to compute an update for the reference frequency $\omega_p(t)$. In the remainder, we omit the time variable t to simplify the notation.

3.4.1 Three-phase droop control

The main contribution of this project is a generalized GFM droop control that combines single-phase droop control for every phase $p \in \mathscr{P}$ with a phase balancing feedback. The equation (3.9) is employed as outer control that generates references to be used by subsequent voltage and current inner control. Considering $(\theta_a^{\mathrm{bal}}, \theta_b^{\mathrm{bal}}, \theta_c^{\mathrm{bal}}) := (0, \frac{2}{3}\pi, -\frac{2}{3}\pi)$ and voltage setpoints $V_p^\star \in \mathbb{R}_{\geq 0}$, the GFM voltage angle and magnitude references $\theta_p^{\mathrm{gfm}} = \delta_p^{\mathrm{gfm}} + \theta_p^{\mathrm{bal}}$ and $V_p^{\mathrm{gfm}} = V_{\delta,p}^{\mathrm{gfm}} + V_p^\star$ are

determined by the outer GFM control (all signals are assumed to be in per unit)

$$\tfrac{\mathrm{d}}{\mathrm{d}t}\delta_p^{\mathrm{gfm}} = \omega_0 - \sum_{l\in\mathscr{P}\setminus p} k_P(\delta_p^{\mathrm{gfm}} - \delta_l^{\mathrm{gfm}}) + m_P(P_p^\star - P_p), \tag{3.9a}$$

$$\tau\tfrac{\mathrm{d}}{\mathrm{d}t}V_{\delta,p}^{\mathrm{gfm}} = -V_{\delta,p}^{\mathrm{gfm}} - \sum_{l\in\mathscr{P}\setminus p} k_Q(V_{\delta,p}^{\mathrm{gfm}} - V_{\delta,l}^{\mathrm{gfm}}) + m_Q(Q_p^\star - Q_p). \tag{3.9b}$$

Here, $P_p^\star \in \mathbb{R}$ and $Q_p^\star \in \mathbb{R}$ are the active and reactive power setpoints and $\omega_0 \in \mathbb{R}_{>0}$ is the nominal frequency. Moreover, $\omega_p^{\mathrm{gfm}} = \omega_0 + \tfrac{\mathrm{d}}{\mathrm{d}t}\delta_p^{\mathrm{gfm}} \in \mathbb{R}$ is the GFM reference frequency for each phase $p \in \mathscr{P}$, $m_P \in \mathbb{R}_{>0}$ is the $P-f$ droop coefficient, $m_Q \in \mathbb{R}_{>0}$ is the $Q-V$ droop coefficient, $\tau \in \mathbb{R}_{>0}$ a lowpass filter time constant, and $k_P \in \mathbb{R}_{\geq 0}$ and $k_Q \in \mathbb{R}_{\geq 0}$ are the phase-balancing feedback gains.

We emphasize that (3.9) reduces to three individual single-phase droop controls if $k_P = k_Q = 0$, i.e., the GFM phase to neutral voltage frequency reference for each phase $p \in \mathscr{P}$ only depend on the active power measurements of phase $p \in \mathscr{P}$. In contrast, if $k_P > 0$, the phase balancing feedback trades off phase voltage frequency unbalance and deviations from the active power setpoints for each phase. If $k_Q > 0$, the phase balancing feedback trades off phase voltage magnitude unbalance and deviations from the reactive power setpoint.

Finally, for large k_P and k_Q, the phase voltage frequency balancing is stiff and the response of generalized three-phase droop control converges to the response of standard GFM droop control as $k_P \to \infty$ and $k_Q \to \infty$. This observation will be formalized in Chapter 5. A block diagram of the generalized $P-f$ droop is shown in Figure 3.3a and a block diagram of the generalized $Q-V$ droop is shown in Figure 3.3b.

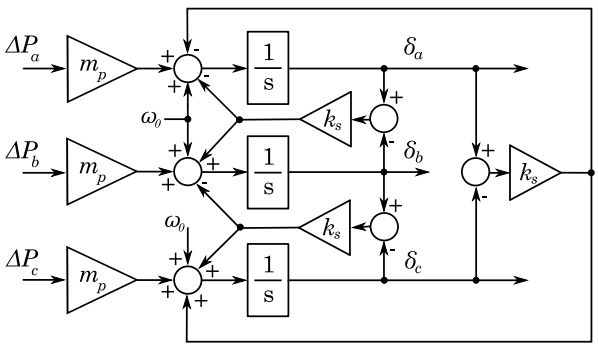

(a) Generalized three-phase $P-f$ droop.

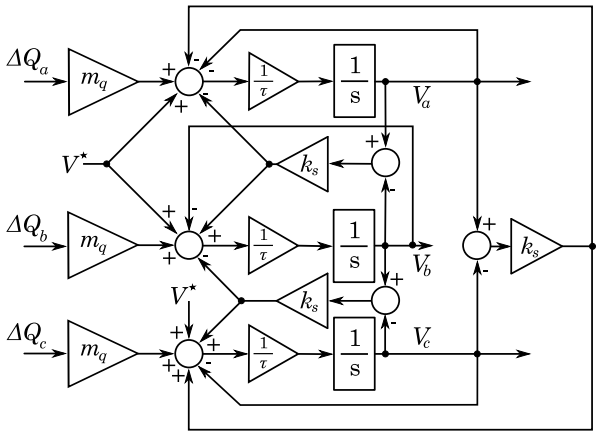

(b) Generalized three-phase $Q-V$ droop.

Figure 3.3: Droop control structure of the generalized three-phase GFM control.

4. Inner controls and current limiting

This chapter presents generalizing standard inner converter controls and current limiting methods to the generalized three-phase control framework developed in this project. First we discuss an extension of the common cascaded dual loop current and voltage control with current reference limiting to the unbalanced case. Then, we discuss threshold virtual impedance current limiting and show how it can be applied to limit phase currents. Finally, a hybrid threshold virtual impedance algorithm is developed that improves upon the performance of threshold virtual impedance current limiting.

4.1 Generalized dual-loop current/voltage control and current limiting

As discussed previously, the generalized three-phase GFM control (3.9) is combined with standard proportional-integral (PI) inner control loops implemented in a synchronous reference frame with reference angle $\theta_p \in \mathbb{S}$ for every phase $p \in \mathscr{P}$ (see Figure 3.2). This generalizes the standard cascaded dual-loop structure (see, e.g., [31]) to allow control of individual phases.

In particular, a voltage controller is used to compute a current reference based on the objective of tracking the GFM reference voltage $v_{p,dq}^{\text{gfm}}$ expressed in a synchronous reference frame with reference angle $\theta_p \in \mathbb{S}$. The control is combined with standard feedforward terms to compensate the impact of the grid current injection $i_{o,p} \in \mathbb{C}$ and is given by

$$i_{p,dq}^{\text{ref}} = i_{o,p,dq} + Y_f v_{p,dq} + G_{\text{PI}}(s)(v_{p,dq}^{\text{gfm}} - v_{p,dq}), \tag{4.1}$$

with a PI controller $G_{\text{PI}}(s)$, filter admittance matrix $Y_f \in \mathbb{R}^{2\times 2}$, and voltage reference $v_{p,dq}^{\text{gfm}} \in \mathbb{R}^2$ (where $\|v_{p,dq}^{\text{gfm}}\| = V_p^{\text{gfm}}$ and $\angle v_{p,dq}^{\text{gfm}} = \theta_p^{\text{gfm}}$).

To limit the current reference provided by the voltage control, a common approach in (positive sequence) GFM control is to apply a so-called circular limiter that limits the magnitude of the reference current $i_{p,dq}^{\text{ref}}$ for all $p \in \mathscr{P}$. This approach is generalized to each phase $p \in \mathscr{P}$ as follows

$$\mathbf{i}_p^{\text{lim}} := \begin{cases} \mathbf{i}_p^{\text{ref}} & \text{if } \|\mathrm{i}_p^{\text{ref}}\| \le I_{\max} \\ i_{\max} \angle \mathbf{i}_p^{\text{ref}} & \text{if } \|\mathrm{i}_p^{\text{ref}}\| > I_{\max} \end{cases}, \tag{4.2}$$

where $I_{\max} \in \mathbb{R}_{>0}$ is maximum phase current magnitude. Then, the limited reference $\mathbf{i}_p^{\lim}$ is provided as a reference to an inner PI current control to track. Notably, the current limiter (4.2) does not clip the current waveform, but adjusts the magnitude of the sinusoidal reference current for every phase to avoid introducing harmonics into the system. Moreover, because it acts on an estimate of a phase current phasor that is obtained without significant delays, it can limit the phase current within a cycle. Finally, for each $p \in \mathscr{P}$, the inner PI current control is given by

$$v_{\mathrm{sw},p,dq} = v_{p,dq} + Z_f i_{p,dq} + G_{\mathrm{PI}}(s)(i_{p,dq}^{\lim} - i_{p,dq}), \tag{4.3}$$

where $Z_f \in \mathbb{R}^{2\times 2}$ denotes the filter impedance matrix and $v_{\mathrm{sw},p,dq} \in \mathbb{R}^2$ is the phase voltage modulated by the VSC.

4.2 Threshold virtual impedance

This section briefly reviews the threshold virtual impedance method for the balanced and critically reflects on its limitations. Then, we illustrate that threshold virtual impedance current limiting can be applied to each phase separately.

To begin with, Figure 4.1 depicts a simplified quasi-steady-state model of a GFM converter with threshold virtual impedance, where the dynamics of the inner-loop control and the $LC-$filter are neglected [33]. The threshold virtual impedance is designed to limit current magnitude $\|i_s\| \coloneqq \sqrt{i_{s,d}^2 + i_{s,q}^2}$[1] at $I_{\max}$ under a three-phase bolted fault at the point of common coupling (PCC) and can be tuned by adjusting its threshold current I_{th} and the X/R ratio $n_{X/R}$ [19]. For a three-phase bolted fault, the magnitude of the voltage drop across the threshold virtual impedance, $\|v^{\mathrm{gfm}} - v\|$, is equal to the nominal voltage V_n (i.e., $V_n = 1$ p.u.) of the converter. The equations for the threshold virtual impedance are given by

$$R_{\mathrm{TVI}} \coloneqq \begin{cases} 0 & \text{if } \|i_s\| < I_{th} \\ k_R\,(\|i_s\| - I_{th}) & \text{if } \|i_s\| \geq I_{th} \end{cases} \tag{4.4a}$$

$$X_{\mathrm{TVI}} \coloneqq n_{X/R} R_{\mathrm{TVI}} \tag{4.4b}$$

with

$$k_R \coloneqq \frac{V_n}{I_{\max}(I_{\max} - I_{th})\sqrt{n_{X/R}^2 + 1}}. \tag{4.5}$$

[1] The most common choice is to limit the filter current i, i.e., $i_s = i$.

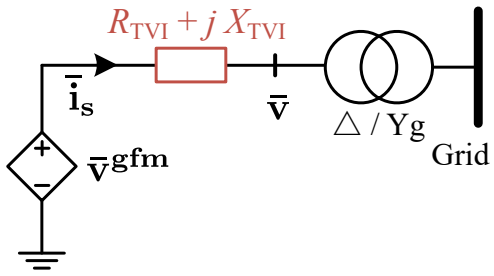

Figure 4.1: Simplified quasi-steady-state model of a GFM converter with threshold virtual impedance (TVI), where a bar denotes the quasi-steady-state of a time domain signal.

Based on Figure 4.1, the magnitude of the quasi-steady-state current $\bar{\mathbf{i}}_\mathbf{s}$ can be calculated by

$$\|\bar{i}_s\| = \frac{\|\bar{v}^{\mathrm{gfm}} - \bar{v}\|}{\sqrt{R_{\mathrm{TVI}}^2 + X_{\mathrm{TVI}}^2}} = \frac{\|\bar{v}^{\mathrm{gfm}} - \bar{v}\|}{R_{\mathrm{TVI}}\sqrt{n_{X/R}^2 + 1}}, \tag{4.6}$$

where $\bar{x}$ denotes the quasi-steady-state of a time domain signal $x(t)$.

Under quasi-steady-state conditions, when the threshold virtual impedance is active, by substituting (4.4a) into (4.6), the relationship between $\|\bar{v}^{\mathrm{gfm}} - \bar{v}\|$ and $\|\bar{i}_s\|$ can be derived as

$$\|\bar{v}^{\mathrm{gfm}} - \bar{v}\| = k_R\sqrt{n_{X/R}^2 + 1}(\|\bar{i}_s\|^2 - I_{th}\|\bar{i}_s\|), \tag{4.7}$$

where $\|\bar{i}_s\| \geq I_{th}$. The control diagram of the threshold virtual impedance (TVI) is shown in the gray dotted box in Figure 4.2.

In this project, a variable transient virtual resistance (VTVR) is implemented to dampen the response of the grid current during transients [20]. The damping factor and the cut-off frequency of the high-pass filter (HPF) are denoted by D and ω_D, respectively. The damping factor D is calculated by

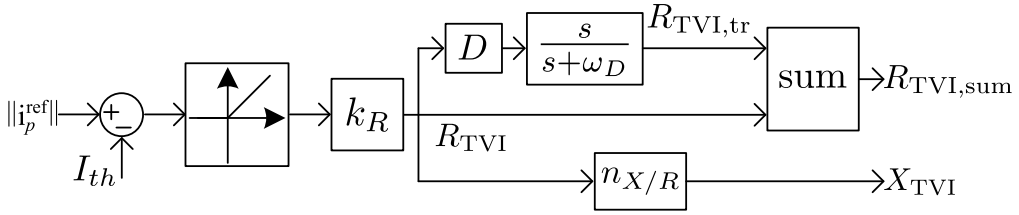

Figure 4.2: Threshold virtual impedance current limiting.

$$D := \frac{n_{X/R}}{n_{X/R,tr}} - 1, \tag{4.8}$$

where $n_{X/R,tr}$ represents the transient X/R ratio. It should be noted that the VTVR only activates during transients, and does not assist the quasi-steady-state current limiting. Next, we briefly illustrate the response of the threshold virtual impedance under large phase angle differences for the parameters provided in Tab. 4.1. Specifically, using (4.7), the quasi-steady-state current magnitude $\|\bar{i}_s\|$ under threshold virtual impedance current limiting can be computed as a function of $\|\bar{v}^{\text{gfm}} - \bar{v}\|$. The corresponding results are illustrated in Figure 4.3. It is important to note that the impedance magnitude of the threshold virtual impedance, $|Z_{\text{TVI}}| := \sqrt{R_{\text{TVI}}^2 + X_{\text{TVI}}^2}$, solely depends on the magnitude of the current i_s without considering any information on the phase of the filter voltage v. Consequently, the threshold virtual impedance is unable to limit the current to $I_{\max}$ when $\|v^{\text{gfm}} - v\| > V_n$ [34], which can be observed in Figure 4.3. This scenario typically occurs due to fault clearing after phase angles have significantly deviated or after phase jumps due to, e.g., connecting or disconnecting a line. In this case, the impedance magnitude calculated using threshold virtual impedance is too small based to effectively limit the current.

Description	Symbol	Value
Threshold current	I_{th}	1.0 p.u.
Maximum current	$I_{\max}$	1.2 p.u.
X/R ratio	$n_{X/R}$	5

Table 4.1: Parameters of Virtual Impedance.

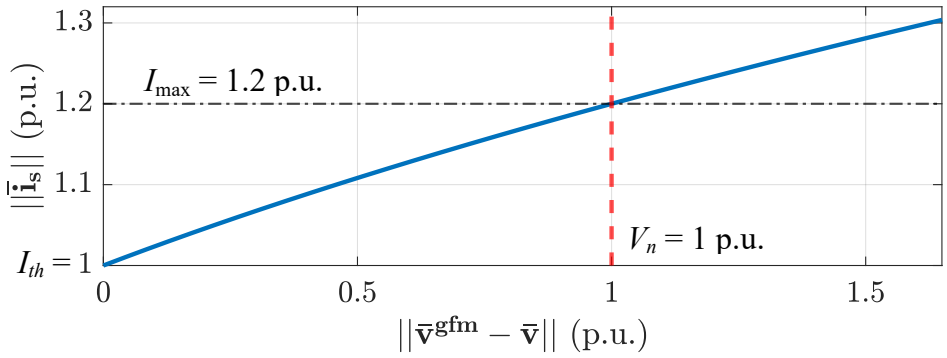

Figure 4.3: The current magnitude $\|\bar{i}_s\|$ for different voltage difference magnitudes $\|\bar{v}^{\text{gfm}} - \bar{v}\|$, when the threshold virtual impedance is active (i.e., $\|\bar{i}_s\| \geq I_{th}$). It can be seen that threshold virtual impedance with standard tuning becomes ineffective when $\|\bar{v}^{\text{gfm}} - \bar{v}\| > V_n$.

4.3 Generalized three-phase threshold virtual impedance

Using the representation of the phase signals in a dq-frame with angle $\theta_p \in \mathbb{S}$, threshold virtual impedance current limiting can be applied to every phase $p \in \mathscr{P}$ by computing the voltage drop over the virtual impedance

$$v_{p,dq,\mathrm{VI}} = \begin{bmatrix} v_{p,d,\mathrm{VI}} \\ v_{p,q,\mathrm{VI}} \end{bmatrix}, \tag{4.9}$$

$$= \begin{bmatrix} R_{\mathrm{TVI,sum}} & X_{\mathrm{TVI}} \\ -X_{\mathrm{TVI}} & R_{\mathrm{TVI,sum}} \end{bmatrix} \begin{bmatrix} i_{o,p,d} \\ i_{o,p,q} \end{bmatrix}. \tag{4.10}$$

Here, $R_{\mathrm{TVI,sum}} \in \mathbb{R}_{>0}$ and $X_{\mathrm{TVI}} \in \mathbb{R}_{>0}$ are computed for every phase using the threshold virtual impedance calculation shown in Figure 4.2. As discussed in [20], the remaining parameters, e.g., $k_R \in \mathbb{R}_{>0}$ and $D \in \mathbb{R}_{>0}$ are determined by the X/R ratio $n_{X/R} \in \mathbb{R}_{>0}$, $I_{\max}$ and I_{th}. Then, the voltage $v_{p,dq,\mathrm{VI}} \in \mathbb{R}^2$ is subtracted from the voltage reference $v^{\mathrm{gfm}}_{p,dq}$, i.e., the reference passed onto inner current control is

$$i^{\mathrm{lim}}_{p,dq} := i_{o,p,dq} + Y_f v_{p,dq} + G_{\mathrm{PI}}(s)(v^{\mathrm{gfm}}_{p,dq} - v_{p,dq,\mathrm{VI}} - v_{p,dq}). \tag{4.11}$$

The overall control algorithm including generalized three-phase droop control and the threshold virtual impedance current limiting for every phase is shown in Figure 4.4.

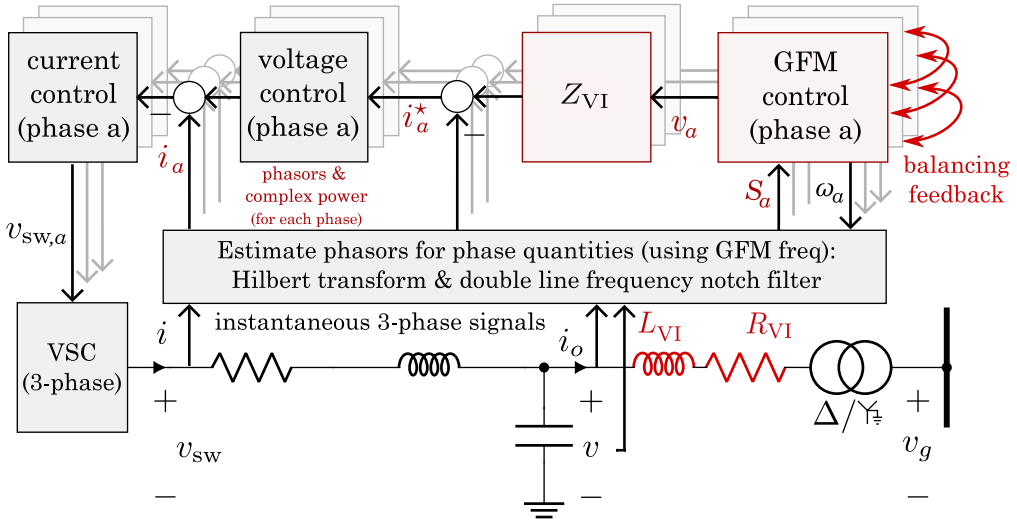

Figure 4.4: Virtual impedance $Z_{VI} := R_{VI} + j\omega^{\mathrm{gfm}}_p L_{VI}$ in the GFM control structure and effective impedance emulation.

4.4 Virtual Impedance Based on Voltage Information

To overcome the limitations of threshold virtual impedance current limiting discussed in Section 4.2, a novel virtual impedance method based on voltage information (VIv) was developed

in this project. The VIv method is specified by

$$R_{\mathrm{VIv}} \coloneqq \frac{1}{\sqrt{n_{X/R}^2+1}} \begin{cases} 0 & \text{if } \|i_s\| < I_{th} \\ \frac{\|v^{\mathrm{gfm}}-v\|}{I_{\max}} & \text{if } \|i_s\| \geq I_{th} \end{cases} \tag{4.12a}$$

$$X_{\mathrm{VIv}} \coloneqq n_{X/R} R_{\mathrm{VIv}}. \tag{4.12b}$$

The VIv utilizes the same parameterization as the threshold virtual impedance, including the maximum current $I_{\max}$, the X/R ratio $n_{X/R}$, and the threshold I_{th}, as the threshold virtual impedance. Notably, the impedance magnitude of the VIv, $|Z_{\mathrm{VIv}}| \coloneqq \sqrt{R_{\mathrm{VIv}}^2 + X_{\mathrm{VIv}}^2}$, is calculated based on the voltage difference $\|v^{\mathrm{gfm}} - v\|$, making it effective in limiting the current for phase jumps, i.e., when voltage phase information is crucial. The control diagram of the VIv depicted in Figure 4.5, incorporates the VTVR similar to the threshold virtual impedance.

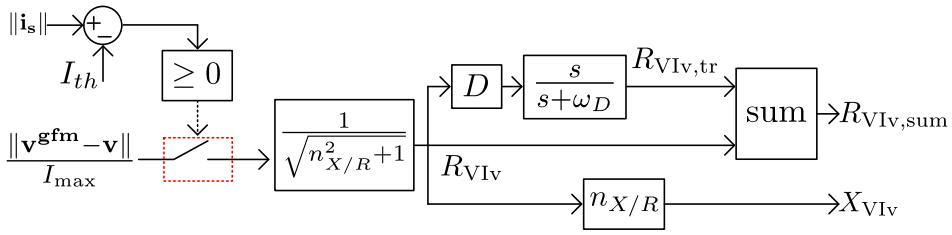

Figure 4.5: Virtual Impedance based on voltage nformation (VIv).

Under quasi-steady-state conditions, when the VIv is active, the magnitude $\|\bar{i}_s\|$ of the current in Figure 4.1 is given by

$$\|\bar{i}_s\| = \frac{\|\bar{v}^{\mathrm{gfm}} - \bar{v}\|}{\sqrt{R_{\mathrm{VIv}}^2 + X_{\mathrm{VIv}}^2}} = \frac{\|\bar{v}^{\mathrm{gfm}} - \bar{v}\|}{R_{\mathrm{VIv}}\sqrt{n_{X/R}^2+1}}, \tag{4.13}$$

where $\|\bar{i}_s\| \geq I_{th}$. Substituting (4.12a) into (4.13), it can be seen that $\|\bar{v}^{\mathrm{gfm}} - \bar{v}\|$ cancels and $\|\bar{i}_s\|$ is always equal to $I_{\max}$. Therefore, the VIv controls the quasi-steady-state current magnitude to $I_{\max}$.

Notably, (4.12) generalizes the approach in [35], which calculates a virtual admittance solely based on voltage magnitude difference (i.e., $\|v^{\mathrm{gfm}}\| - \|\mathbf{v}\|$). This approach requires an additional PI controller to compensate for missing phase information. In contrast, the proposed VIv approach accounts for both the phase and magnitude differences. To the best of the authors' knowledge, no results on the performance of the virtual admittance in [35] for phase jumps have been reported in the literature.

4.4.1 Comparison of TVI and VIv

Under quasi-steady-state conditions, the impedance magnitude of threshold virtual impedance for different voltage difference magnitudes $\|\bar{v}^{\mathrm{gfm}} - \bar{v}\|$ can be derived using (4.4) and (4.7). On the other hand, the impedance magnitude of VIv increases linearly with the voltage difference mag-

nitude based on (4.12). Using the parameters listed in Table 4.1, the impedance magnitude of threshold virtual impedance (TVI) and VIv for different voltage difference magnitudes $\|\bar{v}^{\text{gfm}} - \bar{v}\|$ are illustrated in Figure 4.6.

The quasi-steady-state current magnitude $\|\bar{i}_s\|$ is inversely proportional to the impedance magnitude as shown in (4.6) and (4.13). The VIv is specifically designed to control the quasi-steady-state current magnitude $\|\bar{i}_s\|$ to I_{max}, effectively limiting the current for phase jumps. However, the threshold virtual impedance is unable to limit the current to I_{max} for phase jumps when $\|v^{\text{gfm}} - v\| > V_n$, as depicted in Figure 4.3. Therefore, the VIv provides a larger impedance magnitude when $\|v^{\text{gfm}} - v\| > V_n$, as shown in Figure 4.6. Conversely, the threshold virtual impedance limits the current below I_{max} during short circuit faults when $\|v^{\text{gfm}} - v\| < V_n$, as illustrated in Figure 4.3, while the VIv limits the current to I_{max} with a smaller impedance magnitude. When $\|v^{\text{gfm}} - v\| = V_n$, both threshold virtual impedance and VIv limit the current at I_{max}, resulting in the same impedance magnitude.

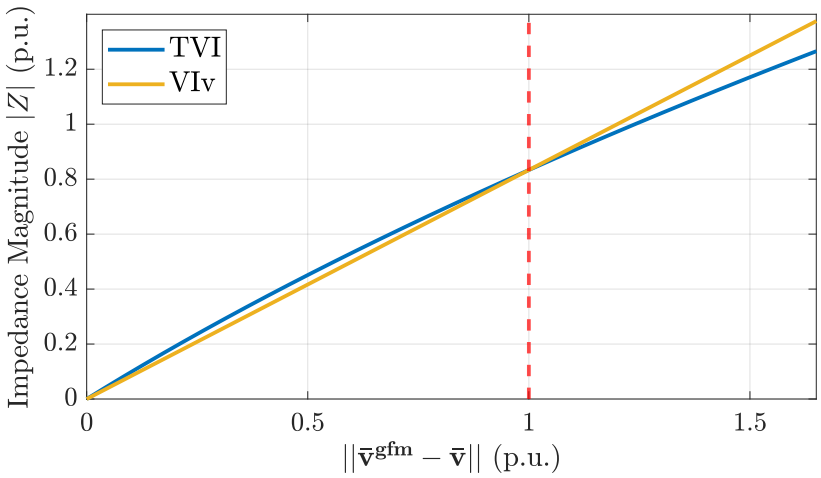

Figure 4.6: Under quasi-steady-state conditions, the impedance magnitude of threshold virtual impedance (TVI) and VIv for different voltage difference magnitudes $\|\bar{v}^{\text{gfm}} - \bar{v}\|$, when $\|\bar{i}_s\| \geq I_{th}$.

4.5 Hybrid Threshold Virtual Impedance (HTVI)

This section presents a hybrid threshold virtual impedance method for GFM converters to effectively limit current under balanced phase jumps and short-circuit faults. To this end, a virtual impedance method based on voltage information (VIv) is proposed to improve the current limiting capability of the standard threshold virtual impedance method for phase jumps (e.g., due to fault clearing or open circuit faults). To leverage the strengths of both threshold virtual impedance and VIv methods, an integrated hybrid threshold virtual impedance method is proposed, which enables reliable current limiting capabilities for both phase jumps and short-circuit faults.

To combine the features of the threshold virtual impedance and the VIv, a hybrid threshold virtual impedance method shown in Figure 4.7 is proposed. During overcurrent situations, both threshold

virtual impedance and VIv are continuously evaluated using the same threshold. The hybrid threshold virtual impedance then uses the maximum impedance magnitude obtained from the threshold virtual impedance and VIv, i.e., $|Z_{\text{HTVI}}| = \max(|Z_{\text{TVI}}|, |Z_{\text{VIv}}|)$. In this way, the hybrid threshold virtual impedance limits the current to $I_{\max}$ for phase jumps when $\|v^{\text{gfm}} - v\| > V_n$ with the help of the VIv. Additionally, when $\|v^{\text{gfm}} - v\| < V_n$, the hybrid threshold virtual impedance limits the current below $I_{\max}$ similar to the threshold virtual impedance. As a result, the proposed hybrid threshold virtual impedance method enhances the FRT capability of the converter under phase jumps and short-circuit faults by fully leveraging the advantages of both threshold virtual impedance and VIv methods.

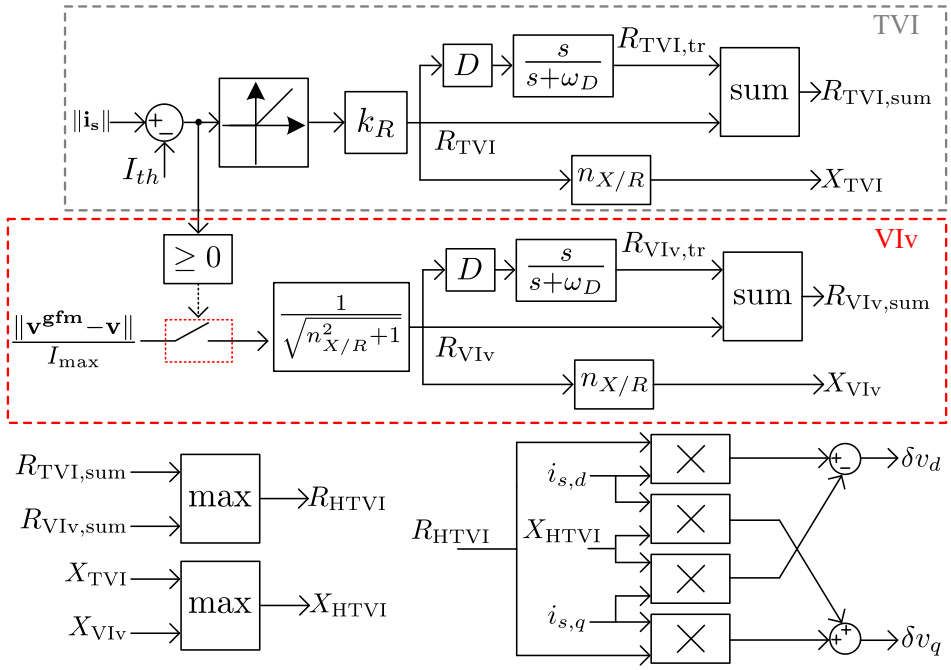

Figure 4.7: Control diagram of the hybrid threshold virtual impedance (HTVI).

4.6 Discussion

The generalized three-phase droop control proposed in this section has three key features. First, the balancing gains k_P and k_Q adjust the trade-off between phase voltage frequency unbalance vs active power unbalance and phase voltage magnitude unbalance vs reactive power unbalance at the converter ac terminal. For example, k_P allows to adjust the contribution of a dc/ac VSC to mitigating angle unbalances in a distribution system. Second, even for large values of k_P and k_Q, a key feature of generalized three-phase droop control is that it (i) tracks voltage frequency/magnitude references for every phase, and (ii) can control and limit the phase currents individually through reference current limiter (4.2), virtual impedance (4.11), or hybrid threshold virtual impedance (see Figure 4.7) (iii) the control explicitly addresses sub-cycle overcurrent by continuously estimating and controlling phase current phasors and limiting their magnitude. Finally, from a theoretical point of view, the proposed control reduces to standard GFM control if the system is balanced. Simulations performed to compare (positive sequence) performance and stability to standard GFM

control only identified significant differences when using negligible phase-balancing gains k_P and k_Q.

5. Stability and steady-state analysis

In this chapter we present results on small-signal stability and the steady-state response of the generalized three-phase droop control. We first summarize results on small-signal stability that highlight that the generalized three-phase droop control ensures small-signal frequency and voltage stability under mild assumptions that are identical to those of regular grid-forming droop control. Subsequently, we analyze the impact of the control gains on the trade off between voltage unbalance and power unbalance at the converter terminal in more detail and establish that (i) the average response of generalized three-phase droop control across the three phases is identical to (positive sequence) grid-forming droop control, (ii) generalized three-phase droop control reduces to (positive sequence) grid-forming droop control in a balanced system.

5.1 Small-signal stability analysis

We begin by briefly summarizing results on small-signal frequency and voltage stability in unbalanced three-phase power systems [36]. To this end, we note that graph-theoretic models commonly used in stability analysis of power systems assume a balanced three-phase network. In this setting, frequency stability is commonly analyzed for balanced systems of grid-forming converters. In particular, small-signal frequency stability of grid-forming converters using (positive sequence) droop control (3.1) interconnected through a quasi-steady-state model of a balanced network is guaranteed if the network is connected. This immediately raises the question if similar small-signal guarantees can be obtained for the generalized three-phase droop control (3.9) and unbalanced three-phase systems.

To answer this question and enable our stability analysis, the work in [36] extends standard graph theoretic models to model unbalanced three-phase networks and standard three-phase transformers. In particular, we model the power system as a connected graph whose nodes represent three-phase buses and edges represent branches such as transmission lines and standard (i.e., $\Delta\Delta$, $\curlyvee\curlyvee$, $\curlyvee_{\!\!+}\curlyvee_{\!\!+}$, $\curlyvee_{\!\!+}\Delta$, and $\curlyvee\Delta$ transformers). For brevity of the presentation we skip the detailed mathematical exposition and refer the reader to [36] for further details. An example for a three-phase system is shown in Figure 5.1. To facilitate the analysis, we partition the system nodes into exterior nodes (i.e., buses with grid-forming converters) and interior nodes (i.e., buses with load). To establish stability for a general unbalanced three-phase network with common three-phase transformers we require the following assumption.

Assumption 1 (interior-exterior node connected network) *The network is interior-exterior node connected, i.e., for any interior node, the subgraph consisting of* $\curlyvee_{\!\!+}\curlyvee_{\!\!+}$ *transformers,* $\curlyvee_{\!\!+}\Delta$ *transformers, and three-phase lines contains a path to an exterior node that traverses all edges from their primary terminal to their secondary terminal.*

Broadly speaking, interior-exterior node connectivity in the sense of Assumption 1 ensures that in-

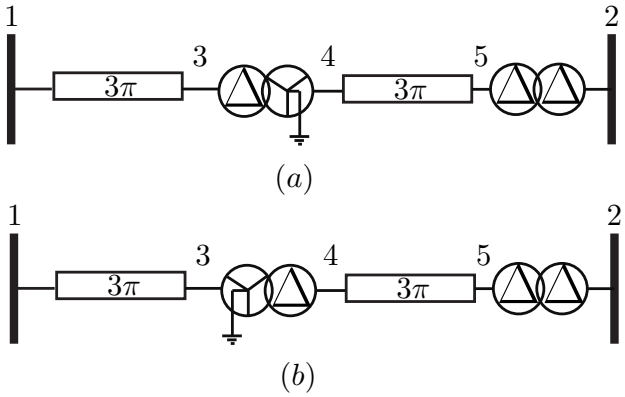

Figure 5.1: The network (a) is interior-exterior node connected because, for every interior node (i.e., 3, 4, and 5), there exists a path to the exterior node 1 containing only three-phase lines and/or a Y-Δ transformers in the correct orientation. The network (b) is not interior-exterior node connected because the paths from the interior nodes 4 and 5 to the exterior nodes 1 or 2 either traverse a ΔΔ transformer or a Y-Δ transformers from its secondary to its primary terminal.

terior node voltages can be recovered from exterior node voltages and bus power injections. Thus, if a network is interior-exterior node connected the interior nodes can be eliminated from the stability analysis through a generalization of Kron reduction. Moreover, interior-exterior node connectivity is related to the notion of an effectively grounded three-phase system encountered in the literature on protection systems that ensures a low impedance path for fault current [37]. Specifically, if the network consisting of the aforementioned branches (i.e., three-phase lines, ΔΔ, YY, Y-Y, Y-Δ, and YΔ transformers) is effectively grounded, then it is interior-exterior node connected. This highlights that assuming the graph to be interior-exterior node connected is not overly restrictive. Similar assumptions have been made in the literature to, e.g., ensure the existence and uniqueness of power flow solutions in three-phase distribution systems with constant power sources and the substation transformer modeled as a slack bus [38, Section IV-C].

The following assumption is required to rule out connections with inconsistent phase shifts or voltage ratios along different branches.

Assumption 2 (Well-posed network) *We assume that*

1. *the network is connected and interior-exterior node connected,*

2. *the number of transformer branches of a specific type, voltage ratio, and orientation traversed by any path between any two nodes is identical.*

Under Assumption 1 and Assumption 2, it can be shown that the overall system with three-phase converters using either positive sequence droop control (3.1) or generalized three-phase droop control (3.9) with $k_P = k_Q = k_s$ and $m_p = m_q/\tau$ is asymptotically stable with respect to a balanced trivial (i.e., nominal voltage and no power flow) solution if one of the following holds: (i) at least

one converter uses positive sequence droop control, (ii) at least one converter uses generalized three-phase droop control with a positive balancing gain k_s, (iii) between any two exterior nodes, there exists at least one path that contains at least one Y⏚Δ branch and all Y⏚Δ branches are traversed in the same orientations.

Notably, this result contains the well-known result for networks of (positive sequence) droop controlled converters connected through three-phase lines as a special case. Crucially, it extends the result to establish that generalized three-phase droop controlled converters with zero phase balancing gain k_s synchronize positive sequence droop controlled converters through three-phase lines, Y⏚Y⏚ transformers, and Y⏚Δ transformers. Moreover, it establishes small-signal frequency and voltage stability of networks of converters using generalized three-phase droop control with positive phase balancing gain k_s. This result shows that, from the viewpoint of small-signal frequency stability, generalized three-phase droop control with $k_s \in \mathbb{R}_{>0}$ does not impose stricter requirements than standard (positive sequence) droop control. Finally, the last condition highlights that networks of generalized three-phase droop control without phase balancing feedback (i.e., $k_s = 0$) synchronize to a balanced solution through specific transformer branches. This result explains the experimental observations in [39] and clarifies the class of three-phase network topologies for which autonomous phase-balancing of three single-phase droop controlled converters connected to a three-phase bus occurs.

5.2 Average dynamics and steady-state analysis

In this section we analyze how the droop coefficients and phase balancing gains and droop gains influence the trade-off between power unbalance and voltage unbalance at the terminals of the GFM converter. To make the notations less verbose, we use $V_{\delta,p}$ for $V_{\delta,p}^{\mathrm{gfm}}$ and δ_p for δ_p^{gfm} for all $p \in \mathscr{P}$.

5.2.1 $Q-V$ droop equation

Vectorizing the generalized three-phase droop control equation (3.9b) and defining $Q_{\delta,p} \coloneqq Q_p^\star - Q_p$ for all $p \in \mathscr{P}$ results in

$$\tau \frac{\mathrm{d}}{\mathrm{d}t} \begin{bmatrix} V_{\delta,a} \\ V_{\delta,b} \\ V_{\delta,c} \end{bmatrix} = - \begin{bmatrix} V_{\delta,a} \\ V_{\delta,b} \\ V_{\delta,c} \end{bmatrix} - k_Q \underbrace{\begin{bmatrix} 2 & -1 & -1 \\ -1 & 2 & -1 \\ -1 & -1 & 2 \end{bmatrix}}_{=:L} \begin{bmatrix} V_{\delta,a} \\ V_{\delta,b} \\ V_{\delta,c} \end{bmatrix} + m_Q \begin{bmatrix} Q_{\delta,a} \\ Q_{\delta,b} \\ Q_{\delta,c} \end{bmatrix}. \tag{5.1}$$

Where $L = L^\mathsf{T}$ is a Laplacian matrix that is used to rewrite the phase-balancing feedback in a compact form. Moreover, we define the transformation matrix

$$T \coloneqq \begin{bmatrix} \frac{1}{3} & \frac{1}{3} & \frac{1}{3} \\ 1 & -1 & 0 \\ 0 & 1 & -1 \end{bmatrix} \tag{5.2}$$

that is used to compute average values across phases as well as the differences between phase a and phase b and phase b and phase c. Applying the transformation T, we obtain

$$\tau \tfrac{\mathrm{d}}{\mathrm{d}t} \begin{bmatrix} V_{\delta,a} \\ V_{\delta,b} \\ V_{\delta,c} \end{bmatrix} = -(I + k_Q L) \begin{bmatrix} V_{\delta,a} \\ V_{\delta,b} \\ V_{\delta,c} \end{bmatrix} + m_Q \begin{bmatrix} Q_{\delta,a} \\ Q_{\delta,b} \\ Q_{\delta,c} \end{bmatrix}, \tag{5.3a}$$

$$\tau \tfrac{\mathrm{d}}{\mathrm{d}t} T \begin{bmatrix} V_{\delta,a} \\ V_{\delta,b} \\ V_{\delta,c} \end{bmatrix} = -T(I + k_Q L)T^{-1} T \begin{bmatrix} V_{\delta,a} \\ V_{\delta,b} \\ V_{\delta,c} \end{bmatrix} + m_Q T \begin{bmatrix} Q_{\delta,a} \\ Q_{\delta,b} \\ Q_{\delta,c} \end{bmatrix}. \tag{5.3b}$$

Simplifying (5.3b), we get

$$\tau \tfrac{\mathrm{d}}{\mathrm{d}t} \begin{bmatrix} \overline{V}_\delta \\ V_{b-a} \\ V_{c-b} \end{bmatrix} = - \begin{bmatrix} 1 & 0 & 0 \\ 0 & 3k_Q + 1 & 0 \\ 0 & 0 & 3k_Q + 1 \end{bmatrix} \underbrace{\begin{bmatrix} \overline{V}_\delta \\ V_{b-a} \\ V_{c-b} \end{bmatrix}}_{= V_{\Delta,p}} + m_Q \begin{bmatrix} \overline{Q}_\delta \\ Q_{b-a} \\ Q_{c-b} \end{bmatrix}. \tag{5.4}$$

Where we used $V_{b-a} \coloneqq V_{\delta,a} - V_{\delta,b} = V_a^\star - V_a - (V_b^\star - V_b)$, $Q_{b-a} \coloneqq Q_{\delta,a} - Q_{\delta,b} = Q_a^\star - Q_a - (Q_b^\star - Q_b)$, $\overline{V}_\delta \coloneqq \frac{1}{3}\sum_{p\in\mathscr{P}}^{i} V_{\delta,i}$ and $\overline{Q}_\delta \coloneqq \frac{1}{3}\sum_{p\in\mathscr{P}}^{i} Q_{\delta,i}$.

Assuming that the references $V_p^\star$ and $Q_p^\star$ are the same for all $p \in \mathscr{P}$, we can simply write $V_{b-a} = V_b - V_a$ and $Q_{b-a} = Q_b - Q_a$. Upon closer inspection of (5.4), we see that the dynamics of the average $\overline{V}_\delta$ only depend on the droop gain m_Q and average reactive power deviation $\overline{Q}_\delta$, i.e., they are identical to the standard (positive sequence) droop control discussed in Section 3.2. On the other hand, the voltage magnitude difference between phases (not to be confused with line-to-line voltages) such as V_{b-a} are dependent on their corresponding reactive power magnitude difference (e.g., Q_{b-a}) and the phase-balancing gains k_Q. To determine the steady state response, we let $\frac{\mathrm{d}}{\mathrm{d}t} V_{\Delta,p} \to 0$ in (5.4) to obtain

$$\begin{bmatrix} \overline{V}_\delta \\ V_{a-b} \\ V_{b-c} \end{bmatrix} = \begin{bmatrix} m_Q & 0 & 0 \\ 0 & -\frac{m_Q}{3k_Q+1} & 0 \\ 0 & 0 & -\frac{m_Q}{3k_Q+1} \end{bmatrix} \begin{bmatrix} \overline{Q}_\delta \\ Q_{a-b} \\ Q_{b-c} \end{bmatrix}. \tag{5.5}$$

It is evident form (5.5) that as $V_{a-b} \to 0$ as $k_Q \to \infty$, establishing that the phase voltage magnitudes will be more balanced for increased k_Q.

5.2.2 $P-f$ droop equation

Similar arguments can be applied to the $P-f$ droop dynamics of generalized three-phase GFM droop equation in (3.9b). Letting $P_{\delta,p} \coloneqq P_p^\star - P_p$ for all $p \in \mathscr{P}$ and vectorizing (3.9a) results in

$$\frac{\mathrm{d}}{\mathrm{d}t}\begin{bmatrix}\delta_a\\ \delta_b\\ \delta_c\end{bmatrix} = \omega_0 I - k_P \begin{bmatrix}2 & -1 & -1\\ -1 & 2 & -1\\ -1 & -1 & 2\end{bmatrix}\begin{bmatrix}\delta_a\\ \delta_b\\ \delta_c\end{bmatrix} + m_P \begin{bmatrix}P_{\delta,a}\\ P_{\delta,b}\\ P_{\delta,c}\end{bmatrix}. \tag{5.6}$$

Defining $\omega_{\delta,p} \coloneqq \frac{\mathrm{d}}{\mathrm{d}t}\delta_p - \omega_0$, it follows that

$$\begin{bmatrix}\omega_{\delta,a}\\ \omega_{\delta,b}\\ \omega_{\delta,c}\end{bmatrix} = -k_P L \begin{bmatrix}\delta_a\\ \delta_b\\ \delta_c\end{bmatrix} + m_P \begin{bmatrix}P_{\delta,a}\\ P_{\delta,b}\\ P_{\delta,c}\end{bmatrix}, \tag{5.7a}$$

$$T\begin{bmatrix}\omega_{\delta,a}\\ \omega_{\delta,b}\\ \omega_{\delta,c}\end{bmatrix} = -k_P T L T^{-1} T \begin{bmatrix}\delta_a\\ \delta_b\\ \delta_c\end{bmatrix} + m_P T \begin{bmatrix}P_{\delta,a}\\ P_{\delta,b}\\ P_{\delta,c}\end{bmatrix}. \tag{5.7b}$$

Assuming that $P_p^\star$ is identical for all $p \in \mathscr{P}$, (5.7b) reduces to

$$\begin{bmatrix}\overline{\omega}_\delta\\ \omega_{a-b}\\ \omega_{b-c}\end{bmatrix} = \begin{bmatrix}0 & 0 & 0\\ 0 & -3k_P & 0\\ 0 & 0 & -3k_P\end{bmatrix}\begin{bmatrix}\overline{\delta}\\ \delta_{a-b}\\ \delta_{b-c}\end{bmatrix} + m_P \begin{bmatrix}\overline{P}_\delta\\ -P_{a-b}\\ -P_{b-c}\end{bmatrix}, \tag{5.8}$$

where $\omega_{a-b} \coloneqq \omega_a - \omega_b$, $P_{a-b} \coloneqq P_a - P_b$, $\overline{\omega}_\delta \coloneqq \frac{1}{3}\sum_{p\in\mathscr{P}}^{i} \omega_{\delta,i}$ and $\overline{P}_\delta \coloneqq \frac{1}{3}\sum_{p\in\mathscr{P}}^{i} P_{\delta,i}$. Following the same steps as in the analysis of the $Q-V$ droop, (5.8) shows that the average frequency deviation $\overline{\omega}_\delta$ is only dependent on average active power deviation $\overline{P}_\delta$, i.e., is identical to (positive sequence) droop control in a balanced system. However, the frequency difference between phases such as ω_{a-b} is dependent on its corresponding active power difference such as P_{a-b}. Using $\omega_{a-b} \coloneqq \frac{\mathrm{d}}{\mathrm{d}t}\delta_{a-b}$ it follows that

$$\frac{\mathrm{d}}{\mathrm{d}t}\delta_{a-b} = -3k_P\delta_{a-b} - m_P P_{a-b}, \tag{5.9}$$

which can be explicitly solved for constant P_{a-b} to obtain

$$\delta_{a-b}(t) = e^{-3k_P(t)}\delta_{a-b}(0) - \frac{m_P}{3k_P}P_{a-b}(1 - e^{-3k_P(t)}). \tag{5.10}$$

In other words, the dynamics of the phase angle differences are input-to-state stable and will converge to $\delta_{a-b}(t) = 0$ in the absence of active power phase imbalance (i.e., $P_{a-b} = 0$).

Moreover, $e^{-3k_P(t)} \to 0$ as $t \to \infty$. Hence, in steady state it follows that

$$\delta_{a-b}(t) = -\frac{m_P}{3k_P} P_{a-b} \tag{5.11}$$

and the same argument holds for the solution of $\delta_{b-c}(t)$.

Therefore, in steady state, (5.8) simplifies to

$$\overline{\omega}_\delta = m_P \overline{P}_\delta, \tag{5.12a}$$

$$\begin{bmatrix} \delta_{a-b} \\ \delta_{b-c} \end{bmatrix} = -\begin{bmatrix} \frac{m_P}{3k_P} & 0 \\ 0 & \frac{m_P}{3k_P} \end{bmatrix} \begin{bmatrix} P_{a-b} \\ P_{b-c} \end{bmatrix}. \tag{5.12b}$$

From (5.12b) it can be inferred that as $k_P \to \infty$, $\delta_{a-b} \to 0$ suggesting that the phase voltage angles tend to be balanced as well. Therefore, along with the results in Section 5.2.1, we conclude that increasing the balancing gains k_P and k_Q will decrease voltage unbalance and, for $k_P \to \infty$ and $k_Q \to \infty$ we expect the voltage magnitude and angle to converge to that of positive sequence droop control.

5.3 Unbalance factors

Next, we analyze the impact of the control gains and load and/or system unbalance on the unbalance factor of the converter terminal voltage. To this end, let V^+ and V^- denote the magnitude of the positive and negative sequence voltage and let $\bar{P} := \frac{1}{3}\sum_{p\in\mathscr{P}} P_p$ and $\bar{Q} := \frac{1}{3}\sum_{p\in\mathscr{P}} Q_p$ denote the average phase power of the VSC. The voltage unbalance factor is given by $V_{\text{UF}} := V^-/V^+$. Moreover, for P_p and Q_p in p.u., we define the power unbalance factors $P_{\text{UF}} := \max_{p\in\mathscr{P}} |P_p - \bar{P}|$, and $Q_{\text{UF}} := \max_{p\in\mathscr{P}} |Q_p - \bar{Q}|$ that resemble standard current unbalance factors commonly used in analysis of electric machines. In this section we establish that, for GFM converter connected to a load and an unbalanced infinite bus, the voltage unbalance V_{UF} of the GFM converter terminal voltage can approximately be bounded based on the power unbalance factors of the load and voltage unbalance factor of the unbalanced infinite bus.

5.3.1 Linearizing voltage unbalance factor

Because V_{UF} is a highly non-linear function with respect to V_p and θ_p, we use a second order Taylor series expansion to approximate V_{UF} as a function of V_p and θ_p with $p \in \mathscr{P}$. To this end, consider the transformation

$$\begin{bmatrix} V^+ \\ V^- \\ V^0 \end{bmatrix} = \frac{1}{3} \begin{bmatrix} 1 & 1 & 1 \\ 1 & \alpha & \alpha^2 \\ 1 & \alpha^2 & \alpha \end{bmatrix} \begin{bmatrix} V_a e^{j\theta_a} \\ V_b e^{j\theta_b} \\ V_c e^{j\theta_c} \end{bmatrix} \tag{5.13}$$

and the function $f(x) = V_{UF}^2 = \frac{(V^-)^2}{(V^+)^2}$ with $x = (\delta_a, \delta_b, \delta_c, V_a, V_b, V_c)$ and $f : \mathbb{R}^6 \to \mathbb{R}$. Also recall from the Section 3.4.1 that $\delta_p = \theta_p - \theta_p^{\text{bal}}$. For $\gamma \in (0,1)$, the second order Taylor approximation of $f(x)$ developed at a balanced operating point is given by

$$V_{\delta,UF}^2 = f(x_0) + \langle \nabla f(x_0), y - x_0 \rangle + \frac{1}{2}(y - x_0)^\mathsf{T} \nabla^2 f(x_0 + \gamma(y - x_0))(y - x_0). \tag{5.14}$$

Substituting $x_0 = (\mathbb{1}_3, \mathbb{0}_3)$, we obtain $f(x_0) = 0$ and $\nabla f(x_0) = \mathbb{0}_6$. Hence, we have that

$$V_{\delta,UF}^2 = \frac{1}{2}(y - x_0)^\mathsf{T} \nabla^2 f(x_0 + \gamma(y - x_0))(y - x_0). \tag{5.15}$$

Notably, we can omit the constant $\frac{1}{2}$ and obtain the upper bound

$$V_{\delta,UF}^2 \leq (y - x_0)^\mathsf{T} \nabla^2 f(x_0)(y - x_0). \tag{5.16}$$

Next, we can use similar techniques to those used in Section 5.2.1 and leverage the transformation

$$\tilde{T} := \begin{bmatrix} T & \mathbb{0}_{3\times 3} \\ \mathbb{0}_{3\times 3} & T \end{bmatrix} \tag{5.17}$$

Next, let $\tilde{x} := \tilde{T}x$. Substituting $\tilde{T}^{-1}\tilde{x} = x$ in (5.16) we obtain

$$V_{\delta,UF}^2 \leq (\Delta x)^\mathsf{T} (\tilde{T}^{-1})^\mathsf{T} \nabla^2 f(x_0) \tilde{T}^{-1} \Delta x, \tag{5.18}$$

where $\Delta x = \tilde{T}(y - x_0)$. Simplifying $H := (\tilde{T}^{-1})^\mathsf{T} \nabla^2 f(x_0) \tilde{T}^{-1}$ we obtain,

$$H = \begin{bmatrix} 0 & 0 & 0 & 0 & 0 & 0 \\ 0 & \frac{2}{9} & -\frac{1}{9} & 0 & 0 & \frac{\sqrt{3}}{9} \\ 0 & -\frac{1}{9} & \frac{2}{9} & 0 & -\frac{\sqrt{3}}{9} & 0 \\ 0 & 0 & 0 & 0 & 0 & 0 \\ 0 & 0 & -\frac{\sqrt{3}}{9} & 0 & \frac{2}{9} & -\frac{1}{9} \\ 0 & \frac{\sqrt{3}}{9} & 0 & 0 & -\frac{1}{9} & \frac{2}{9} \end{bmatrix}. \tag{5.19}$$

Also, note that $\Delta x = (\overline{\delta}, \delta_{a-b}, \delta_{b-c}, \overline{V}, V_{a-b}, V_{b-c})$ and that H can be further simplified by omitting

the rows and columns from (5.19) that are zero. This is supported by the intuition that average values do not affect the unbalance factor and results in

$$\tilde{H} := \begin{bmatrix} \frac{2}{9} & -\frac{1}{9} & 0 & \frac{\sqrt{3}}{9} \\ -\frac{1}{9} & \frac{2}{9} & -\frac{\sqrt{3}}{9} & 0 \\ 0 & -\frac{\sqrt{3}}{9} & \frac{2}{9} & -\frac{1}{9} \\ \frac{\sqrt{3}}{9} & 0 & -\frac{1}{9} & \frac{2}{9} \end{bmatrix}, \tag{5.20}$$

(5.21)

and $\Delta\tilde{x} := (\delta_{a-b}, \delta_{b-c}, V_{a-b}, V_{b-c})$.

Substituting $\tilde{H}$ and $\Delta\tilde{x}$ in (5.16), we obtain the approximate bound

$$V^2_{\delta,UF} \leq (\Delta\tilde{x})^{\mathsf{T}} \tilde{H} \Delta\tilde{x}. \tag{5.22}$$

Summarizing, (5.22) is linearized version of V^2_{UF} near a balanced operating point x_0 with reduced dimension of the state vector from $\mathbb{R}^6$ to $\mathbb{R}^4$ with the help of coordinate transformation $\tilde{T}$. Next, we will further bound $V^2_{\delta,UF}$ as a function of load and grid voltage unbalance.

5.3.2 Standalone GFM converter with unbalanced load

When the GFM converter is connected to an unbalanced load as shown in Figure 5.2, the corresponding voltage magnitude and angle unbalance is captured through (5.5) and (5.8).

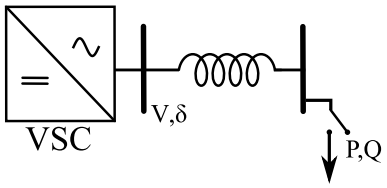

Figure 5.2: GFM converter connected to an unbalanced load.

Using (5.22) and recalling the relationship between active power and power angle given in (5.12b) and reactive power and voltage given in (5.5), we obtain

$$V^2_{\delta,UF} \leq \begin{bmatrix} P_{a-b} \\ P_{b-c} \\ Q_{a-b} \\ Q_{b-c} \end{bmatrix}^{\mathsf{T}} \begin{bmatrix} \frac{m_P}{3k_P} & 0 & 0 & 0 \\ 0 & \frac{m_P}{3k_P} & 0 & 0 \\ 0 & 0 & \frac{m_Q}{3k_Q+1} & 0 \\ 0 & 0 & 0 & \frac{m_Q}{3k_Q+1} \end{bmatrix}^{\mathsf{T}} \tilde{H} \begin{bmatrix} \frac{m_P}{3k_P} & 0 & 0 & 0 \\ 0 & \frac{m_P}{3k_P} & 0 & 0 \\ 0 & 0 & \frac{m_Q}{3k_Q+1} & 0 \\ 0 & 0 & 0 & \frac{m_Q}{3k_Q+1} \end{bmatrix} \begin{bmatrix} P_{a-b} \\ P_{b-c} \\ Q_{a-b} \\ Q_{b-c} \end{bmatrix}, \tag{5.23}$$

$$\leq \begin{bmatrix} P_{a-b} \\ P_{b-c} \\ Q_{a-b} \\ Q_{b-c} \end{bmatrix}^{\mathsf{T}} \begin{bmatrix} \frac{2m_P^2}{81k_P^2} & -\frac{m_P^2}{81k_P^2} & 0 & \frac{\sqrt{3}m_P m_Q}{27k_P(3k_Q+1)} \\ -\frac{m_P^2}{81k_P^2} & \frac{2m_P^2}{81k_P^2} & -\frac{\sqrt{3}m_P m_Q}{27k_P(3k_Q+1)} & 0 \\ 0 & -\frac{\sqrt{3}m_P m_Q}{27k_P(3k_Q+1)} & \frac{2m_Q^2}{9(3k_Q+1)^2} & -\frac{m_Q^2}{9(3k_Q+1)^2} \\ \frac{\sqrt{3}m_P m_Q}{27k_P(3k_Q+1)} & 0 & -\frac{m_Q^2}{9(3k_Q+1)^2} & \frac{2m_Q^2}{9(3k_Q+1)^2} \end{bmatrix} \begin{bmatrix} P_{a-b} \\ P_{b-c} \\ Q_{a-b} \\ Q_{b-c} \end{bmatrix}. \tag{5.24}$$

Next, let

$$\gamma_1 \coloneqq \frac{m_P^2}{81k_P^2} \begin{bmatrix} P_{a-b} & P_{b-c} \end{bmatrix} \begin{bmatrix} 2 & -1 \\ -1 & 2 \end{bmatrix} \begin{bmatrix} P_{a-b} \\ P_{b-c} \end{bmatrix}, \tag{5.25}$$

$$\gamma_2 \coloneqq \frac{m_Q^2}{(3k_Q+1)^2} \begin{bmatrix} Q_{a-b} & Q_{b-c} \end{bmatrix} \begin{bmatrix} 2 & -1 \\ -1 & 2 \end{bmatrix} \begin{bmatrix} Q_{a-b} \\ Q_{b-c} \end{bmatrix}, \tag{5.26}$$

$$\gamma_3 \coloneqq \frac{2\sqrt{3}m_P m_Q}{27k_P(3k_Q+1)} \begin{bmatrix} Q_{a-b} & Q_{b-c} \end{bmatrix} \begin{bmatrix} 0 & -1 \\ 1 & 0 \end{bmatrix} \begin{bmatrix} P_{a-b} \\ P_{b-c} \end{bmatrix}. \tag{5.27}$$

Then, (5.24) can be equivalently be represented as,

$$V_{\delta,UF}^2 \leq \gamma_1 + \gamma_2 + \gamma_3. \tag{5.28}$$

The remainder of this section will maximize γ_1 through γ_3 for a given load unbalance factor to determine an upper bound on $V_{\delta,UF}^2$.

Since, the power imbalances are bounded by this their respective power unbalance factors, they serve as the constraints for maximizing $\gamma_1 + \gamma_2 + \gamma_3$. Recalling the definition of P_{UF} and Q_{UF}, we obtain

$$P_{UF} \geq \frac{1}{3} \begin{bmatrix} 2 & -1 & -1 \\ -1 & 2 & -1 \\ -1 & -1 & 2 \\ -2 & 1 & 1 \\ 1 & -2 & 1 \\ 1 & 1 & -2 \end{bmatrix} \begin{bmatrix} P_a \\ P_b \\ P_c \end{bmatrix}, \tag{5.29}$$

$$\geq \frac{1}{3} \begin{bmatrix} 2 & -1 & -1 \\ -1 & 2 & -1 \\ -1 & -1 & 2 \\ -2 & 1 & 1 \\ 1 & -2 & 1 \\ 1 & 1 & -2 \end{bmatrix} T^{-1} \begin{bmatrix} \overline{P} \\ P_{a-b} \\ P_{b-c} \end{bmatrix}, \tag{5.30}$$

$$\geq \frac{1}{3}\begin{bmatrix} 0 & 1 & 1 \\ 0 & -2 & 1 \\ 0 & 1 & -2 \\ 0 & -1 & -1 \\ 0 & 2 & -1 \\ 0 & -1 & 2 \end{bmatrix}\begin{bmatrix} \overline{P} \\ P_{a-b} \\ P_{b-c} \end{bmatrix}. \tag{5.31}$$

By removing the average element out of (5.31) we get

$$P_{UF} \geq \frac{1}{3}\begin{bmatrix} 1 & 1 \\ -2 & 1 \\ 1 & -2 \\ -1 & -1 \\ 2 & -1 \\ -1 & 2 \end{bmatrix}\begin{bmatrix} P_{a-b} \\ P_{b-c} \end{bmatrix}. \tag{5.32}$$

The reactive power unbalance power factor can analogously be used to bound phase power unbalances as follows

$$Q_{UF} \geq \frac{1}{3}\begin{bmatrix} 1 & 1 \\ -2 & 1 \\ 1 & -2 \\ -1 & -1 \\ 2 & -1 \\ -1 & 2 \end{bmatrix}\begin{bmatrix} Q_{a-b} \\ Q_{b-c} \end{bmatrix}. \tag{5.33}$$

The set (5.32) is shown in Figure 5.3a for $P_{UF} = 0.5$. By observation, the constraints can be over-approximated as shown in Figure 5.3b.

The over-approximation shown in Figure 5.3b results in the set

$$P_{UF} \geq \frac{1}{2}\begin{bmatrix} 1 & 0 \\ 0 & 1 \\ -1 & 0 \\ 0 & -1 \end{bmatrix}\begin{bmatrix} P_{a-b} \\ P_{b-c} \end{bmatrix}. \tag{5.34}$$

Similarly, the constraint set (5.33) can be over-approximated by

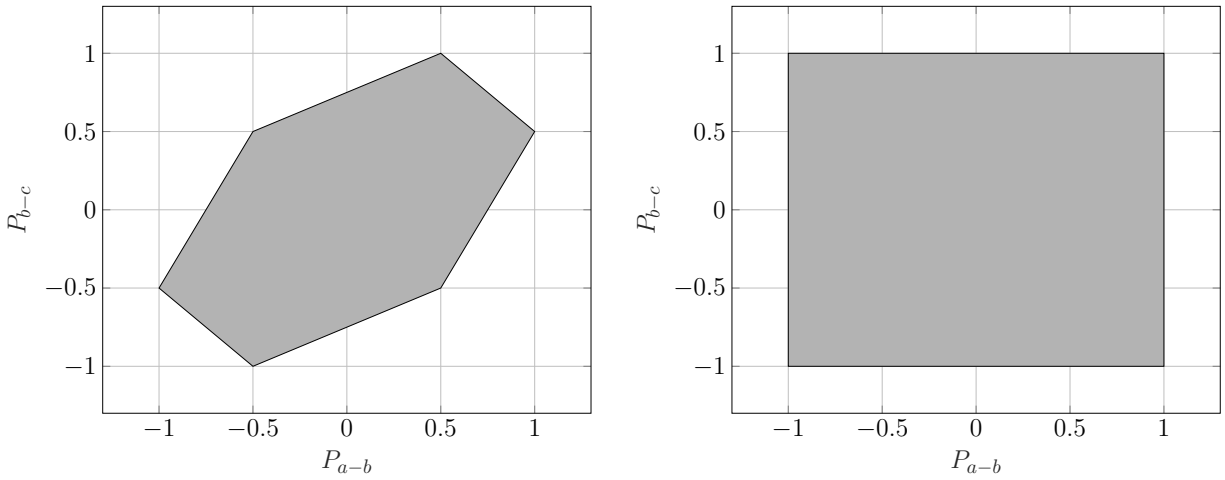

(a) Constraint set for $P_{UF} = 0.5$.

(b) Over-approximated constraint set for $P_{UF} = 0.5$.

Figure 5.3: Constraint sets for the maximization of power unbalances for a given power unbalance factor.

$$Q_{UF} \geq \frac{1}{2} \begin{bmatrix} 1 & 0 \\ 0 & 1 \\ -1 & 0 \\ 0 & -1 \end{bmatrix} \begin{bmatrix} Q_{a-b} \\ Q_{b-c} \end{bmatrix}. \tag{5.35}$$

Let $\mathscr{X}$ denote the constraint set given in (5.32) and (5.33) as shown in Figure 5.3a. Then, we can bound $V^2_{\delta,UF}$ as follows

$$V^2_{\delta,UF} \leq \max_{x \in \mathscr{X}} (\gamma_1 + \gamma_2 + \gamma_3). \tag{5.36}$$

Moreover, it holds that

$$V^2_{\delta,UF} \leq \max_{x \in \mathscr{X}} \gamma_1 + \max_{x \in \mathscr{X}} \gamma_2 + \max_{x \in \mathscr{X}} \gamma_3. \tag{5.37}$$

Next, let $\tilde{\mathscr{X}}$ denote the set given in the (5.34) and (5.35) as depicted in Figure 5.3b. Because $\mathscr{X} \subset \tilde{\mathscr{X}}$, it holds that

$$V_{\delta,UF}^2 \leq \max_{x\in\tilde{\mathscr{X}}} \gamma_1 + \max_{x\in\tilde{\mathscr{X}}} \gamma_2 + \max_{x\in\tilde{\mathscr{X}}} \gamma_3. \tag{5.38}$$

Finally, analytically solving the maximization problems in (5.38) results in the bound

$$V_{U\delta,UF}^2 \leq \frac{2m_p^2}{27k_P^2} P_{UF}^2 + \frac{2m_Q^2}{3(3k_Q+1)^2} Q_{UF}^2 + \frac{16\sqrt{3}m_P m_Q}{27k_Q(3k_Q+1)} P_{UF}Q_{UF}. \tag{5.39}$$

This bounds the voltage unbalance factor of the GFM converter through power unbalance factors of the load in a standalone GFM converter with an unbalanced load system. This result highlights that increasing the droop coefficients $m_p \in \mathbb{R}_{>0}$ and $m_q \in \mathbb{R}_{>0}$ increases the impact of unbalanced load on the converter terminal voltage unbalance. At the same time, increasing the phase-balancing gains $k_P \in \mathbb{R}_{>0}$ and $k_Q \in \mathbb{R}_{>0}$ decreases the impact of unbalanced load on the converter terminal voltage unbalance.

5.3.3 GFM converter connected to unbalanced grid

Next, we investigate how grid voltage unbalances impact the voltage unbalance at the converter terminal. To this end, we consider the connection of a GFM converter to an unbalanced infinite bus depicted in Figure 5.4.

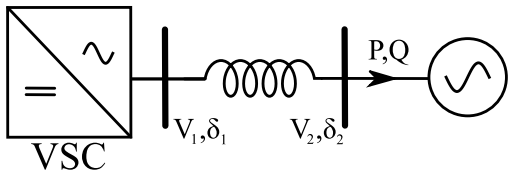

Figure 5.4: GFM converter is connected to an unbalanced grid.

In particular, we will derive conditions under which the voltage unbalance factor at the converter terminal can be related to the voltage unbalance factor at the infinite bus and the converter control gains. It is expected that the voltage unbalance at the converter admits a direct relationship with the infinite bus unbalance and the balancing gains $k_P \in \mathbb{R}_{>0}$ and $k_Q \in \mathbb{R}_{>0}$. For the system shown in Figure 5.4 it holds that

$$\begin{bmatrix} V_{1,a-b} \\ V_{1,b-c} \end{bmatrix} = -\begin{bmatrix} \frac{m_Q}{3k_Q+1} & 0 \\ 0 & \frac{m_Q}{3k_Q+1} \end{bmatrix} \begin{bmatrix} Q_{a-b} \\ Q_{b-c} \end{bmatrix}, \tag{5.40a}$$

$$\begin{bmatrix}\delta_{1,a-b}\\ \delta_{1,b-c}\end{bmatrix} = -\begin{bmatrix}\frac{m_P}{3k_P} & 0\\ 0 & \frac{m_P}{3k_P}\end{bmatrix}\begin{bmatrix}P_{a-b}\\ P_{b-c}\end{bmatrix}. \tag{5.40b}$$

By linearizing the reactive power flow across the inductor shown in Figure 5.4 at the nominal operating point $V^\star$ and $\delta^\star$, we obtain

$$\begin{bmatrix}V_{1,a-b}\\ V_{1,b-c}\end{bmatrix} = -\begin{bmatrix}\frac{m_Q}{3k_Q+1} & 0\\ 0 & \frac{m_Q}{3k_Q+1}\end{bmatrix}\begin{bmatrix}b(V_{1,a-b}-V_{2,a-b})\\ b(V_{1,b-c}-V_{2,b-c})\end{bmatrix}, \tag{5.41a}$$

$$\begin{bmatrix}V_{1,a-b}\\ V_{1,b-c}\end{bmatrix} = \begin{bmatrix}\frac{bm_Q}{3k_Q+bm_Q+1} & 0\\ 0 & \frac{bm_Q}{3k_Q+bm_Q+1}\end{bmatrix}\begin{bmatrix}V_{2,a-b}\\ V_{2,b-c}\end{bmatrix}. \tag{5.41b}$$

Similarly, linearizing the active power results in

$$\begin{bmatrix}\delta_{1,a-b}\\ \delta_{1,b-c}\end{bmatrix} = -\begin{bmatrix}\frac{m_P}{3k_P} & 0\\ 0 & \frac{m_P}{3k_P}\end{bmatrix}\begin{bmatrix}b(\delta_{1,a-b}-\delta_{2,a-b})\\ b(\delta_{1,b-c}-\delta_{2,b-c})\end{bmatrix}, \tag{5.42a}$$

$$\begin{bmatrix}\delta_{1,a-b}\\ \delta_{1,b-c}\end{bmatrix} = \begin{bmatrix}\frac{bm_P}{3k_P+bm_P} & 0\\ 0 & \frac{bm_P}{3k_P+bm_P}\end{bmatrix}\begin{bmatrix}\delta_{2,a-b}\\ \delta_{2,b-c}\end{bmatrix}. \tag{5.42b}$$

Combining (5.41b) and (5.42b) results in

$$\begin{bmatrix}\delta_{1,a-b}\\ \delta_{1,b-c}\\ V_{1,a-b}\\ V_{1,b-c}\end{bmatrix} = F\begin{bmatrix}\delta_{2,a-b}\\ \delta_{2,b-c}\\ V_{2,a-b}\\ V_{2,b-c}\end{bmatrix}, F := \begin{bmatrix}\frac{bm_P}{3k_P+bm_P} & 0 & 0 & 0\\ 0 & \frac{bm_P}{3k_P+bm_P} & 0 & 0\\ 0 & 0 & \frac{bm_Q}{3k_Q+bm_Q+1} & 0\\ 0 & 0 & 0 & \frac{bm_Q}{3k_Q+bm_Q+1}\end{bmatrix}. \tag{5.43a}$$

Using (5.43a) to bound the voltage unbalance factor, we obtain

$$V^2_{\delta,1,UF} = z_2^\mathsf{T}\tilde{H}_F z_2, \tag{5.44}$$

where $\tilde{H}_F := F^\mathsf{T}\tilde{H}F$ and $z_2 := (\delta_{2,a-b}, \delta_{2,b-c}, V_{2,a-b}, V_{2,b-c})$. Moreover, for a given value of $V_{\delta,2,UF}$

we have

$$V^2_{\delta,2,UF} = \tfrac{1}{2} z_2^{\mathsf{T}} \tilde{H} z_2. \tag{5.45}$$

Our goal is to bound $V^2_{\delta,1,UF}$ as a function of $V^2_{\delta,1,UF}$. This requires bounding $z_2^{\mathsf{T}} \tilde{H}_F z_2$ in terms of $z_2^{\mathsf{T}} \tilde{H} z_2$. However, if there exists z_2 such that $z_2 \in \ker \tilde{H}$ but $z_2 \notin \mathcal{N}(\tilde{H}_F)$, then $V^2_{\delta,2,UF} = 0$ but $V^2_{\delta,1,UF} \neq 0$. It follows that the GFM converter terminal voltage unbalance cannot be bounded based on the grid voltage unbalance factor. In other words, the desired bound can only be obtained if $\tilde{H}$ and $\tilde{H}_F$ have the same null space. This is true when

$$\frac{bm_Q}{3k_Q + bm_Q + 1} = \frac{bm_P}{3k_P + bm_P}. \tag{5.46}$$

In this case, the bounds on the GFM voltage unbalance factor can be directly computed as

$$V^2_{\delta,1,UF} \leq 2 \left(\frac{bm_P}{3k_P + bm_P} \right)^2 V^2_{\delta,2,UF}, \tag{5.47}$$

which again illustrates that increasing the phase balancing gains $k_P \in \mathbb{R}_{\geq 0}$ and $k_Q \in \mathbb{R}_{\geq 0}$ decreases the voltage unbalance at the converter terminal.

6. Distributed cold start under unbalanced conditions

This chapter introduces a strategy for distributed cold starts of distribution feeders under unbalanced conditions, obviating the necessity for centralized coordination. To begin with, an advanced load relay is introduced, serving as a crucial component in achieving this goal. Moreover, a cold start methodology employing GFM converters for unbalanced conditions is outlined.

6.1 Advanced load relay

To enhance the cold start capability, an advanced load relay is modeled in this study. The load relay combines frequency and voltage relay functionalities and is designed to trip/reset the breaker based on predefined operating ranges and specified delay times. By utilizing individual reset delay times for load relays, the system operator can achieve a gradual energization/connection of loads during the cold start process, thereby mitigating the risk of Cold Load Pickup [28] associated with inrush currents. The load relays continuously measure the frequency and voltage as indicators of the grid's state, eliminating the need for additional communication with the inverters during the cold start process. For example, when the frequency stays within a predefined deviation range ($\pm$0.9Hz) from the nominal frequency for the connection waiting time $T_{\text{freq,con}}$, the load relay will connect the load. Conversely, if the frequency deviates from this predefined range for the disconnection waiting time $T_{\text{freq,dis}}$, the load relay will disconnect the load. During the cold start process, these waiting times are initialized to avoid simultaneous switching on/off of all loads, and can be modified based on the priority of operation.

6.2 GFM cold start logic

The GFM converter, equipped with the generalized three-phase droop control, emerges as a promising solution for cold start operation under unbalanced system. Subsequent to a blackout event, the first GFM converter initiates a gradual increase in its terminal voltage by ramping up its voltage magnitude setpoints. This method achieves soft transformer energization and eliminates the inrush current. To prevent power oscillation among different GFM converters, a PLL is used before connecting the second GFM converter. The PLL initially synchronizes with the voltage at the connection point of the second converter. Following a suitable synchronization period, the angle measured by the PLL is used to initialize the GFM control of the second GFM converter.

With the synchronization and connection of all GFM converters in the system, the advanced relays are activated. As a result, the gradual reconnection of loads occurs based on local voltage and frequency information. Importantly, throughout the cold start process, the active power can be effectively shared by GFM converters.

7. Case study: MV/HV system

This chapter describes a benchmark system developed in this project to illustrate and verify the unbalanced fault ride through capabilities of the controls developed in this project. Moreover, the system is used to study the interactions of GFM converters with distance protection typically encountered in transmission systems.

7.1 Benchmark system

To illustrate the results, we use a high-fidelity EMT simulation of a two-level dc/ac VSC connected to an infinite bus through a 1 km medium voltage line, a 40 km double circuit high voltage transmission line, and step up transformers. The system parameters are provided in Table. 7.1. Unless noted otherwise, an averaged converter model is used and the control is implemented at a sampling rate of 10 kHz. The system is shown in Figure 7.1. For reasons of space, the converter output filter is not shown explicitly. An unbalanced load of 1 MW is placed at the inverter bus and used to evaluate the response to unbalanced load. Moreover, faults are simulated on the upper transmission line of the double transmission line and cleared by opening a breaker on this line. Lastly the system is connected to an infinite bus through an impedance computed based on the desired equivalent short circuit ratio (SCR) of the overall system.

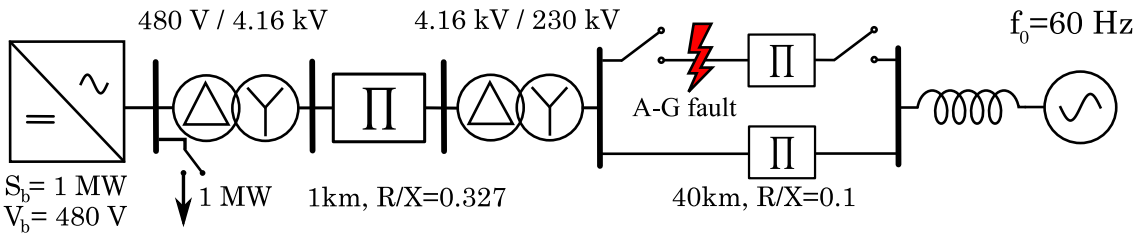

Figure 7.1: Test system with a low-voltage VSC connected to a weak ac system through a distribution line, double circuit transmission line, and a step-up transformer.

7.2 Unbalanced load

To validate the analysis in Chapter 5, we first illustrate the response of the converter to an unbalanced load for various controls and control parameters.

7.2.1 Generalized three phase droop control

To illustrate the role of the phase balancing gain k_P and k_Q, Fig 7.2 shows the steady-state voltage and power unbalance factors at the VSC terminal for an unbalanced delta connected constant

Table 7.1: Parameters used in the model illustrated in Figure 7.1

Description	Value
Phase balancing gain k_P	1e5 p.u.
Phase balancing gain k_Q	1e5 p.u.
Phase balancing gain $k_s \ni k_P = k_Q \coloneqq k_s$	1e5 p.u.
Inverter base power S_b	1e6 W
Inverter base voltage V_b	480 V
Inverter filter capacitor	0.05 p.u.
Inverter filter inductor	0.1 p.u.
Inverter filter resistor	0.01 p.u.
Inverter active power set point per phase	0.1 p.u.
Inverter reactive power set point per phase	0 p.u.
Inverter voltage set point per phase	1 p.u.
Threshold current limit I_{th}	1 p.u.
Absolute current limit $I_{\max}$	1.2 p.u.
TVI constant k_R	0.817
TVI constant D	15.66
TVI constant $n_{X/R}$	5
TVI HPF cut-off frequency ω_D	100 Hz
$P-f$ droop m_P	0.05 p.u.
$Q-V$ droop m_Q	0.05 p.u.
Base frequency	60 Hz
Medium voltage line resistance	0.21 Ω/km
Medium voltage line inductance	17e-4 H/km
Medium voltage line capacitance	1e-8 F/km
Medium voltage line base voltage	4.16e3 V
Medium voltage line length	1 km
High voltage line resistance	0.03 Ω/km
High voltage line inductance	7.95e-4 H/km
High voltage line capacitance	10e-9 F/km
High voltage line base voltage	230e3
High voltage line length	10 km

impedance load[1] at the VSC bus (see Figure 7.1). The results show the expected trade off between voltage unbalance and power unbalance, i.e., increasing the phase balancing gain $k_P = k_Q \coloneqq k_s$ reduces voltage unbalance V_{UF} but increases power unbalance P_{UF} and Q_{UF}.

[1] Relative to the load between phase a and b, the load between phase b and c is 20% lower and the load between phase a and c is 20% higher

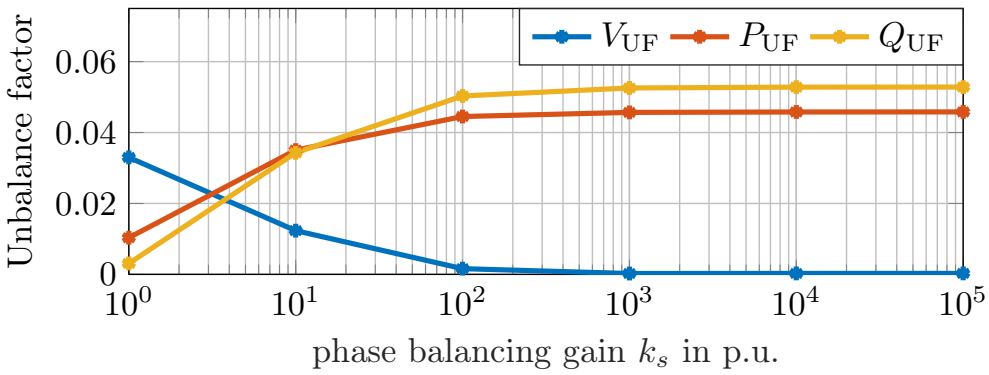

Figure 7.2: Steady-state unbalance factors for an unbalanced load at the VSC terminal as a function of the phase balancing gain k_s.

This result is consistent with equations (5.5) and (5.12b) obtained from analytical steady state analysis. As k_Q increases, the voltage imbalance between the phases reduces irrespective of the reactive power imbalance. Similarly, as k_P increase the angle difference between different phases also abets irrespective of the active power difference.

7.2.2 Positive-negative sequence droop control

To illustrate the droop response of the positive-negative sequence droop control, the positive-negative sequence droop control (3.2a) and (3.2c) that implements droop based on negative sequence currents has been implemented in the system shown in Fig 7.1. In this implementation the positive and negative sequence components of the voltage are added and converted to *abc* by applying the Fortescue transformation and extracting the real part of the voltage phasors for each phase. This reference is then tracked by the generalized three-phase cascaded inner current and voltage loops. The steady state response to same unbalanced load as used in the previous section are shown Figure 7.3.

As shown in Figure 7.3a, the negative sequence voltage increases linearly with the negative sequence droop gain m_Q^- and, as expected, the negative sequence current reduces linearly. However, as shown in Figure 7.3b, the negative sequence power Q^- increases in magnitude as a nonlinear function of the negative sequence reactive power droop gain m_Q^- increases. Similarly, the negative sequence active power P^- increases as a function of the negative sequence reactive power droop gain m_Q^-. This result highlights the nonlinear relationship of the power and current and its impact on the positive-negative sequence droop control (3.2a) and (3.2c).

Overall, we observe that, due to the aforementioned nonlinearity, the tuning of the negative sequence droop coefficients is not intuitive. Moreover, in simulation, we observe that large coefficients that would result in significant reduction in negative sequence current or power can result in instability, particularly under weak grid coupling. These challenges have not been observed with the generalized three-phase droop control.

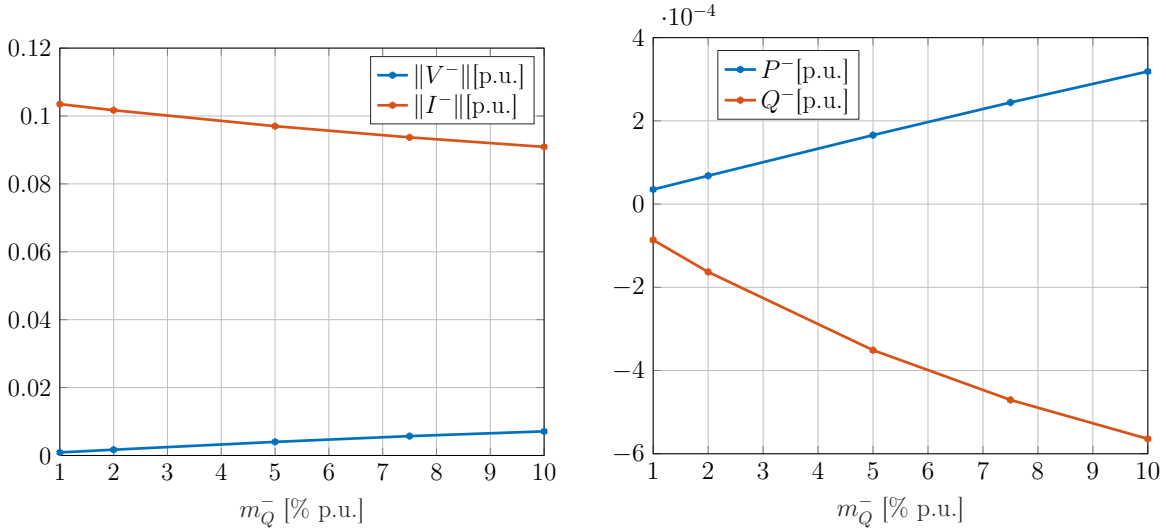

(a) Negative sequence current magnitude $\|I^-\|$ and voltage magnitude $\|V^-\|$.

(b) Negative sequence active power P^- and reactive power Q^-.

Figure 7.3: Steady-state response to an unbalanced load at the VSC terminal as a function of the negative sequence reactive droop gain m_Q^{-1}.

7.3 Balanced short-circuit faults and phase jumps

To compare the fault-ride-through capability of various virtual impedance methods under balanced conditions, we again use the system illustrated in Figure 7.4. For this case study, the load at the converter terminal is disconnected. To clearly illustrate the difference between the virtual impedance current limiting methods presented in Chapter 4, we consider a balanced short circuit fault and phase jumps and employ the standard (positive sequence) droop control with inner loops in a synchronous reference frame as shown in Figure 3.1.

An aggregate model is used for the GFM converter, representing multiple converter modules with lower power ratings. The GFM converter is connected to an infinite bus through a 1 km medium voltage line and 40 km double circuit high voltage transmission line through step-up transformers. The short-circuit ratio (SCR) at the PCC is 2.78. A switching model for the converter is used to accurately capture the dynamic behavior of the system. The system and control parameters utilized in the simulations are listed in Table 4.1 and Table 7.2.

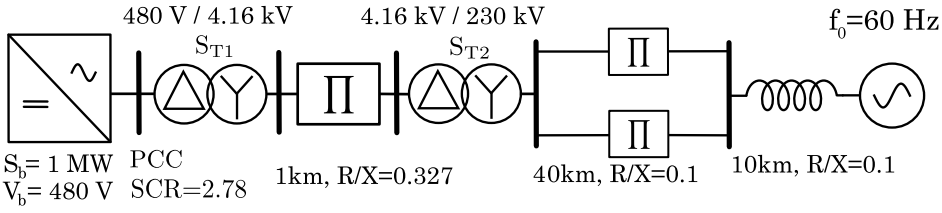

Figure 7.4: Test system with a low-voltage GFM converter connected to a weak ac system through a distribution line, double circuit transmission line, and a step-up transformer.

Table 7.2: System and Control Parameters.

Description	Symbol	Value
Inverter base power	S_b	1 MVA
Inverter base voltage	V_b	480 V
Filter inductance	L_f	0.156 p.u.
Filter capacitance	C_f	0.023 p.u.
Switching frequency	f_{sw}	10 kHz
Transient X/R ratio	$n_{X/R,tr}$	0.8
Cut-off frequency of HPF for VTVR	ω_D	1000 rad/s
PI coefficients of voltage controller	$K_{P,v}$ and $K_{I,v}$	0.83 p.u., 0.23 p.u.
PI coefficients of current controller	$K_{P,c}$ and $K_{I,c}$	1.11 p.u., 0.24 p.u.

7.3.1 Grid voltage phase jump

In the simulation results shown in Figure 7.5, a phase angle change of -110° is imposed at the grid voltage. The responses of the filter current, filter voltage, $\|v^{\text{gfm}} - v\|$, virtual reactance X_{vi}, active power, and reactive power for the GFM converter operating with threshold virtual impedance (TVI), VIv, and hybrid threshold virtual impedance (HTVI) are analyzed. After the occurrence of the phase jump, $\|v^{\text{gfm}} - \mathbf{v}\| > V_n$ holds, and the threshold virtual impedance (TVI) fails to limit the fault current to 1.2 p.u., which persists for a duration of 364 ms. This result aligns with the analysis presented in Figure 4.3. In contrast, the VIv effectively limits the fault current to 1.2 p.u. after the phase jump, exhibiting a larger impedance magnitude compared to the threshold virtual impedance (TVI). However, oscillations in current magnitude are observed during the initial 30 ms of the fault.

In contrast, the hybrid threshold virtual impedance (HTVI) effectively limits the current magnitude under the phase jump, similar to the VIv. It also reduces the current below 1.2 p.u. faster than the VIv when $\|v^{\text{gfm}} - v\| < V_n$, with the help of the threshold virtual impedance (TVI). Additionally, the hybrid threshold virtual impedance (HTVI) exhibits a well-damped current response, similar to the threshold virtual impedance (TVI). This supports the intuition that the hybrid threshold virtual impedance (HTVI) combines the advantages of the threshold virtual impedance (TVI) and VIv. As a result, the hybrid threshold virtual impedance (HTVI) outperforms the threshold virtual impedance (TVI) and VIv under phase jumps, offering improved performance and FRT capability.

When the phase jump occurs, a spike in the filter voltage is observed, reaching a peak value of 1.8 p.u., lasting for 1 ms. This spike is caused by the large phase shift in the grid voltage. After the occurrence of the phase jump, the active and reactive power exhibits a brief but large transient before returning to the normal operating point. This behavior is a result of the resynchronization between the GFM converter and the grid. However, despite these transients, the system maintains transient stability, and the current is effectively limited as desired.

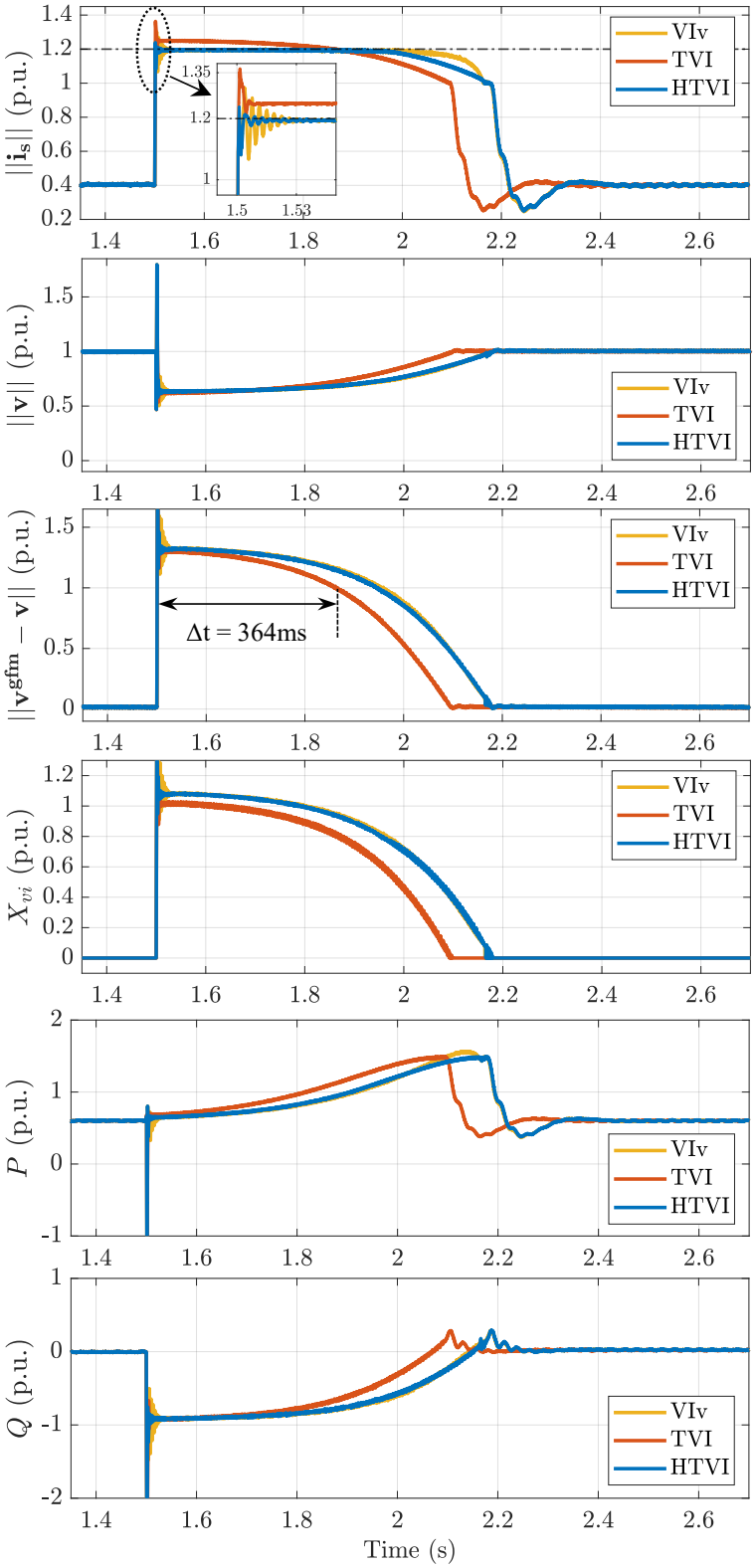

Figure 7.5: Response of filter current, filter voltage, $\|v^{\text{gfm}} - v\|$, virtual reactance X_{vi}, active power, and reactive power for the GFM converter with TVI, VIv, and HTVI under a -110° grid voltage phase jump at 1.5 s.

7.3.2 Three-phase short-circuit fault

Next, a three-phase ground fault is imposed on the distribution line of the test system depicted in Figure 7.4, causing a 0.8 p.u. voltage drop at the PCC. The fault is cleared after 400 ms. The responses of the filter current, filter voltage, $\|v^{\text{gfm}} - \mathbf{v}\|$, virtual reactance X_{vi}, active power, and reactive power for the GFM converter operating with threshold virtual impedance (TVI), VIv, and hybrid threshold virtual impedance (HTVI) are shown in Figure 7.6.

The threshold virtual impedance (TVI) effectively limits the fault current at 1.16 p.u. (i.e., smaller than the maximum of 1.2 p.u.) since the fault is not located at the PCC (i.e., $\|v^{\text{gfm}} - v\| < V_n$). In contrast, the VIv controls the steady-state fault current at 1.2 p.u. with a smaller impedance magnitude compared to the threshold virtual impedance (TVI). During the fault-inception period, the threshold virtual impedance (TVI) demonstrates better performance, while the VIv exhibits a higher transient current with a peak value of 1.41 p.u. and oscillations during the first 15 ms of the fault period.

Subsequent to clearing the fault at $t = 1.90$ s, the current limiting capability of the threshold virtual impedance (TVI) is compromised again as $\|v^{\text{gfm}} - v\| > V_n$. Consequently, the fault current remains above 1.2 p.u. for a duration of 210 ms. In contrast, the VIv continues to limit the current at 1.2 p.u., providing a larger impedance magnitude. However, the VIv shows oscillations in the current for 30 ms and a slower response in reducing the current below 1.2 p.u. compared to the threshold virtual impedance (TVI).

Notably, the hybrid threshold virtual impedance (HTVI) maintains the performance of the threshold virtual impedance (TVI) during the short-circuit fault to limit the fault current at 1.16 p.u. with a well-damped current response. Once the fault is cleared, the hybrid threshold virtual impedance (HTVI) limits the current to 1.2 p.u., similar to the VIv. It also reduces the current below 1.2 p.u. faster than the VIv when $\|v^{\text{gfm}} - v\| < V_n$, with the help of the threshold virtual impedance (TVI). These results demonstrate that the hybrid threshold virtual impedance (HTVI) method improves the fault ride through capability of the GFM converter by leveraging the strengths of both the threshold virtual impedance (TVI) and VIv methods.

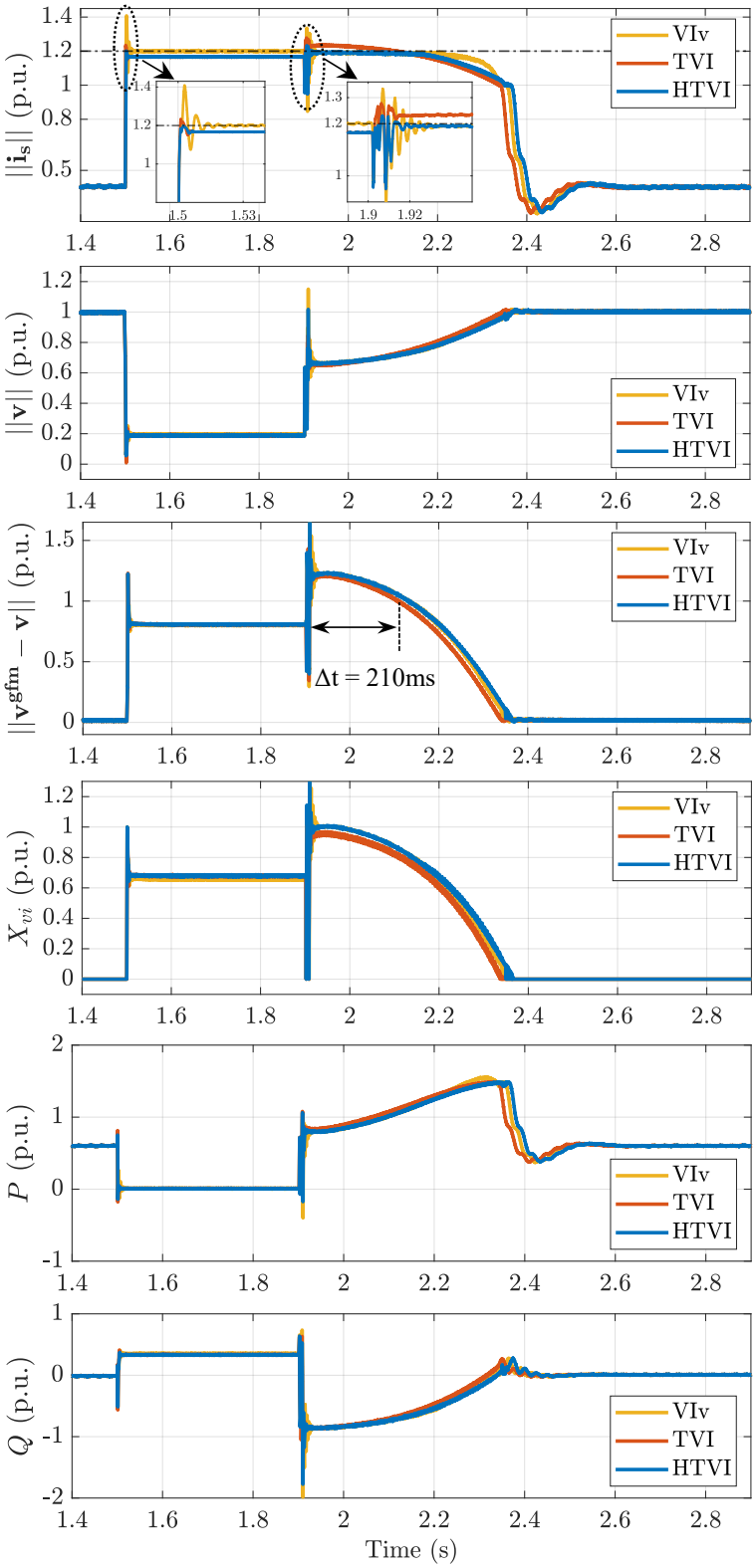

Figure 7.6: Response of filter current, filter voltage, $\|v^{\text{gfm}} - v\|$, virtual reactance X_{vi}, active power, and reactive power for the GFM converter with TVI, VIv, and HTVI during a three-phase ground fault at 1.5 s. The fault is cleared after 400 ms.

7.4 Single line-to-ground fault

To illustrate the impact of separate voltage/current control and current limiting for every phase on unbalanced fault ride through, we disconnect the load at the VSC terminal and consider a zero impedance line-to-ground fault for phase a of a transmission line (see Figure 7.1).

7.4.1 Current saturation algorithm (CSA)

Generalized three phase droop control

We first investigate the response of the generalized three-phase droop control with three-phase cascaded dual-loop inner controls. Figure 7.7 shows the resulting VSC terminal voltage magnitude $V_p = \|\mathbf{v}_p\|$, VSC phase current magnitude $I_p = \|\mathbf{i}_p\|$, active power P_p, and reactive power Q_p for every phase $p \in \mathscr{P}$.

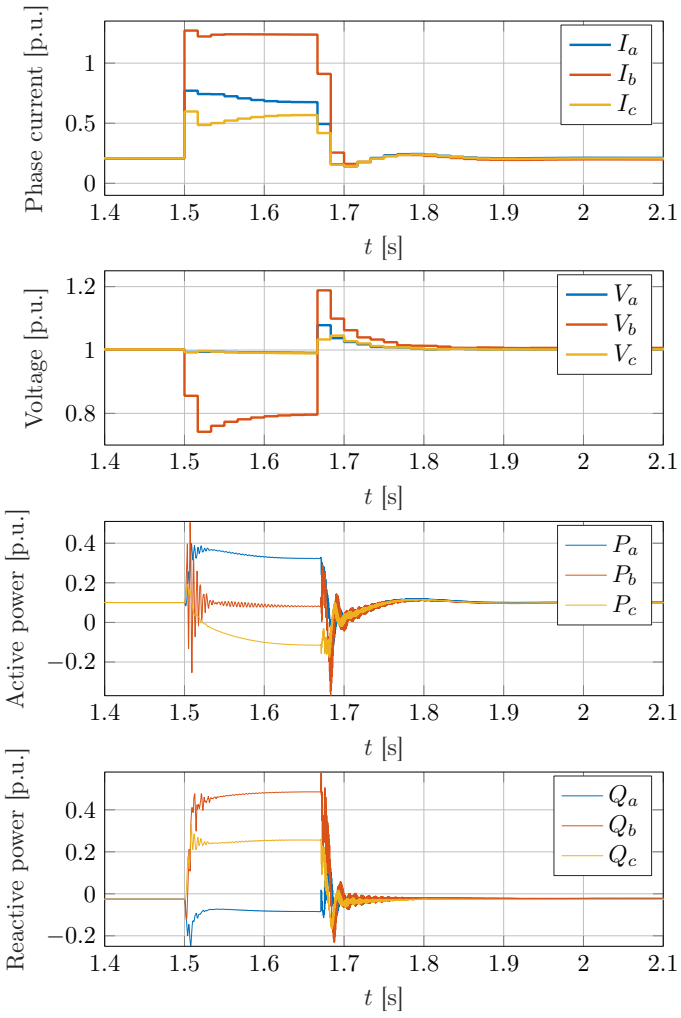

Figure 7.7: Response of the generalized droop control to a phase a to ground fault on a transmission line at $t = 1.5$ s with CSA current limiting. The fault is cleared after ten cycles by disconnecting the faulted line.

Because the magnitudes of phase currents and voltages are not well-defined within a cycle, the maximum magnitude over one cycle is shown. We use $k_s = 10^5$ p.u., i.e., the outer GFM control is configured to resemble standard droop control (sec. 3.2), and the fault is applied at $t = 1.5$ s and cleared after ten cycles by disconnecting the faulted line. Notably, due to the converters' transformer connection, the fault applied to phase a of the transmission line, is effectively mapped to phase b at the VSC terminal.

It can be seen that the current reference limiter (4.2) and PI current control (4.3) successfully limit the current magnitude to $I_{\max} = 1.2$ p.u. within one cycle. Notably, by controlling the current phasor for every phase, the proposed control explicitly handles sub-cycle overcurrent. Once the fault is cleared a significant resynchronization transient is observed that can be attributed to controller windup in the voltage loop (4.1) and GFM angle dynamics (3.9a) and is a known challenge of reference current limiting.

To further illustrate the positive impact of the generalized three-phase GFM control, the simulation study has been repeated with standard droop control using the dual-loop inner control structure. In this case, the current and voltage waveforms are severely distorted because the VSC aims to impose balanced phase currents and a balanced voltage at its terminal. However, under its current limits, the VSC cannot maintain a balanced voltage at the terminal during the unbalanced fault. Terminal voltage waveforms for both controls are shown in Figure 7.8.

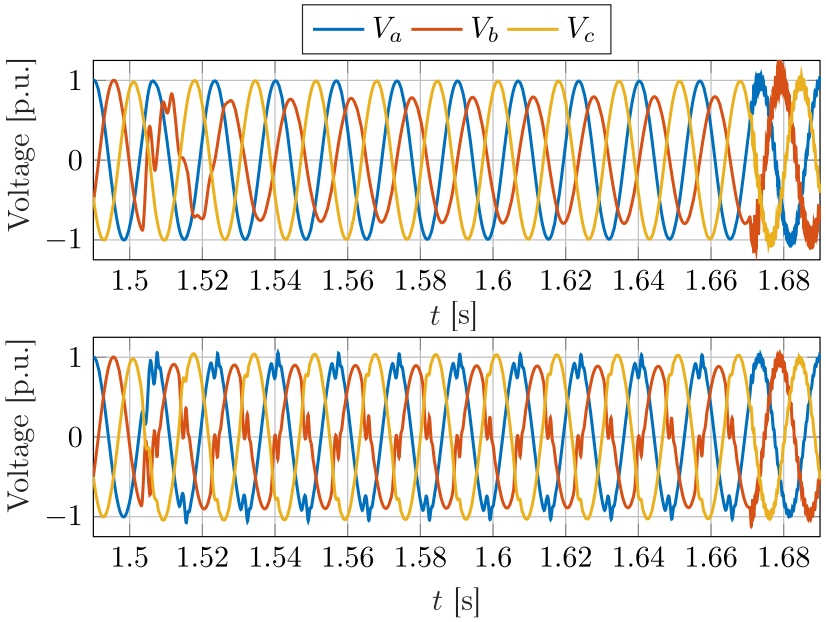

Figure 7.8: VSC voltages during a phase a to ground fault using generalized three-phase droop control with dual-loop current/voltage control for every phase (top) and standard droop control and dual-loop current/voltage control (bottom).

It can be seen that the proposed control successfully imposes a sinusoidal ac voltage waveform at the terminals of the VSC that is unbalanced to limit the current. In contrast, standard droop control

results in a highly distorted voltage.

In the above simulations, once the fault is cleared it is observed that system returns to a stable operating point. However, for longer fault durations the current reference limiting may preclude resynchronization once the fault is cleared. To illustrate the impact of the balancing gain on the clearing time of the GFM converter we determined the critical clearing time in simulation for different values of $k_P = k_Q = k_s$. In addition, we also varied the SCR of the grid coupling to observe the trend of critical clearing time from weak grid to strong grid. Figure. 7.9 shows that the critical clearing time increases (measured in ac cycles at the nominal frequency) increases as k_s decreases. In other words, by allowing voltage phase angles for every phase to deviate from each other, the critical clearing time is increased because a healthy phase can maintain synchronization with the grid. Additionally, as SCR increases the critical clearing time increases.

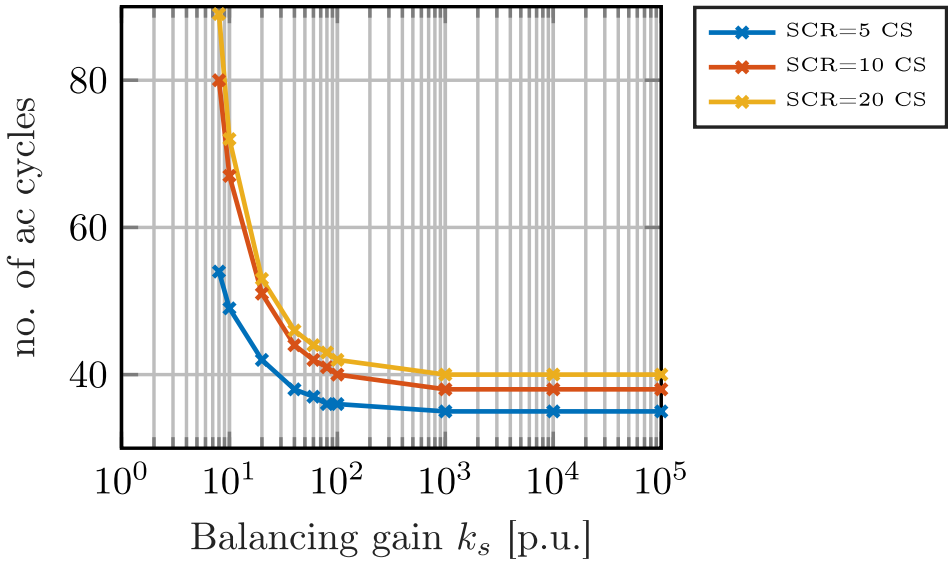

Figure 7.9: Critical clearing time as a function of the phase balancing gain $k_P = k_Q = k_s$ for different grid coupling strengths. The vertical axis shows critical clearing in ac cycles at the nominal frequency.

Positive-negative sequence droop control

Next, we discuss simulation results for the positive-negative sequence droop control (3.2a) and (3.2c) that again provides a reference to separate inner control loops for each phase.

The response of the GFM converter to the phase a to ground fault used in this section is shown in Figure 7.10. Because the fault response is largely determined by the current limiter, the response is very similar to that of the generalized three-phase droop control shown in Figure 7.7. The current is again successfully limited during the fault. However, a significantly larger resynchronization transient and ringing are observed. This response is attributed to the nonlinear response of the negative sequence droop and its predominantly balanced reference voltage even under severe unbalance.

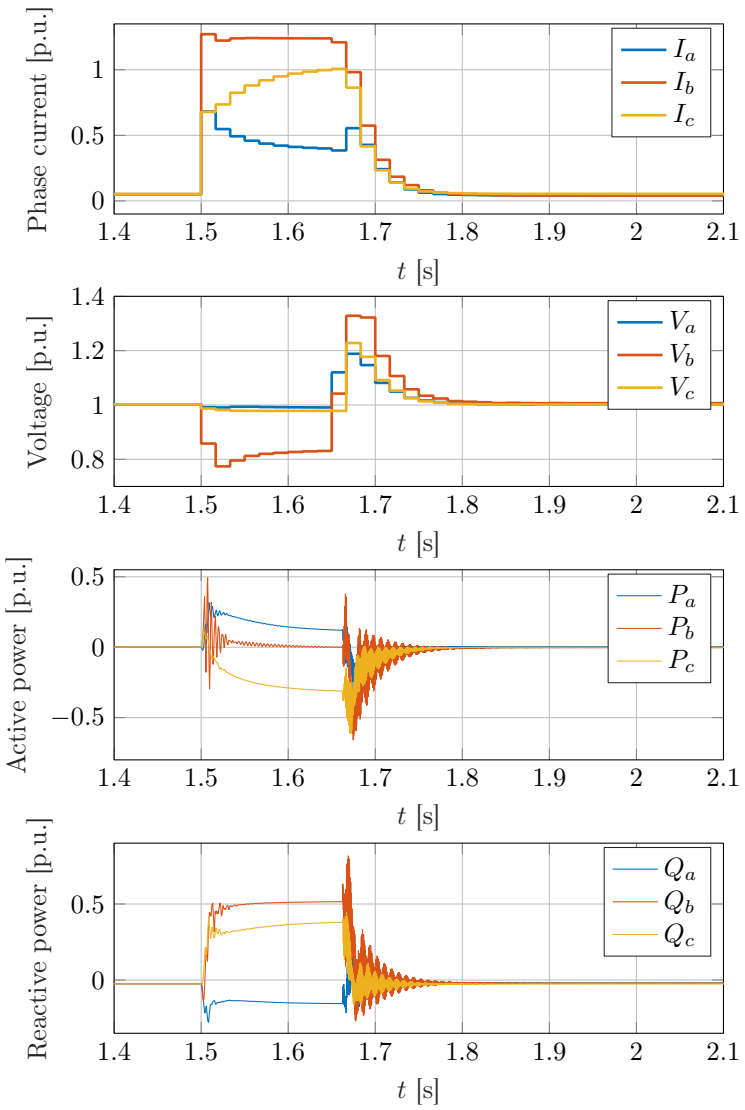

Figure 7.10: Response of positive-negative sequence droop control to a phase a to ground fault on a transmission line at $t = 1.5$ s, with CSA current limiting. The fault is cleared after ten cycles by disconnecting the faulted line.

7.4.2 Threshold virtual impedance (TVI)

Next, we investigate the response of the generalized three-phase droop control with threshold virtual impedance current limiting (4.9) implemented separately for every phase. The response of the GFM converter to a phase a to ground fault is captured in the Figure 7.1. Notably, Figure 7.11 shows that the fault current is limited more aggressively compared to that of CSA. Moreover, the voltage overshoot after clearing the fault is significantly reduced. This can be attributed to the fact that no integrator wind up occurs in the inner voltage loop when threshold virtual impedance is used.

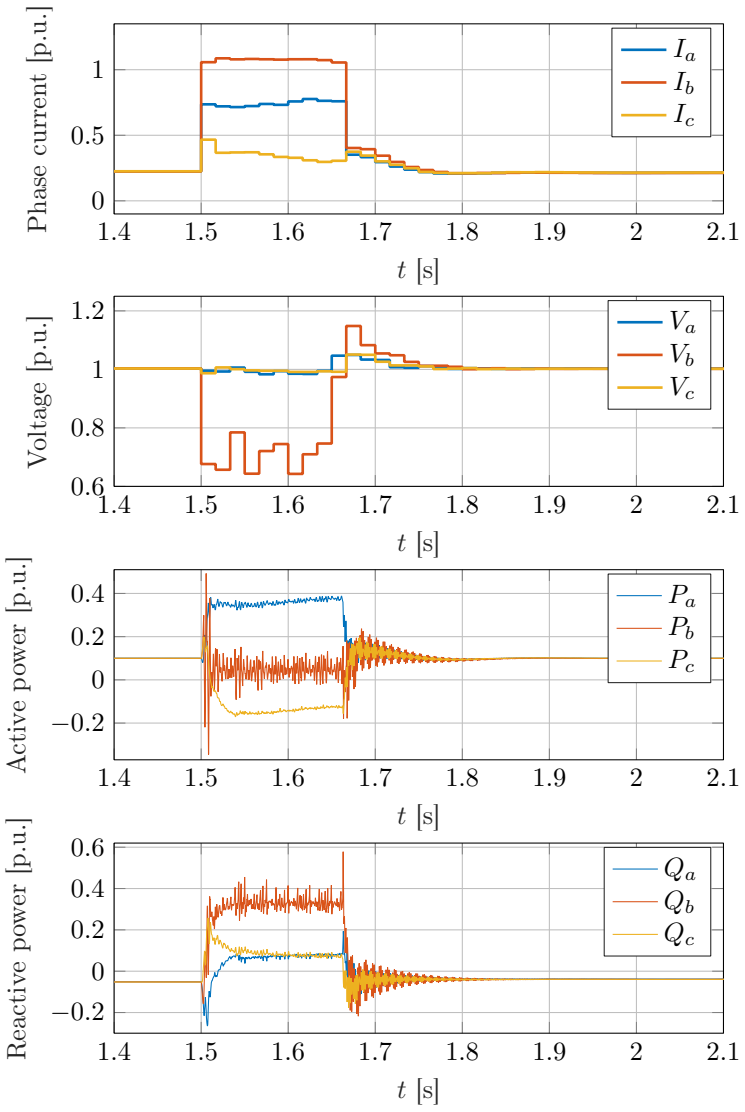

Figure 7.11: Response of generalized droop control to a phase a to ground fault on a transmission line at $t = 1.5$ s, with TVI current limiting. The fault is cleared after ten cycles by disconnecting the faulted line.

On the other hand, both active and reactive powers, exhibit significant ringing that can be attributed

to transient stability challenges that are commonly observed with threshold virtual impedance current limiting. Nonetheless, threshold virtual impedance current limiting results in improved fault-ride-through capabilities.

Finally, we emphasize that using threshold virtual impedance current limiting results in a significantly increased critical clearing time that is several times longer than the critical clearing time when using reference current limiting.

Finally, we compare the resynchronization time after the fault is cleared. Figure 7.12 shows the resynchronization time to within 5% of the nominal operating point after the fault is cleared. Results are provided for both CSA and TVI as a function of the phase balancing gain $k_P = k_Q = k_s$ for various grid coupling strengths. Figure 7.12 shows that, while there is no obvious trend, with respect to SCR and current limiting method, the resynchronization time reduces when the phase balancing gain k_s is increased. Therefore, along with the trade-off between phase power and phase voltage imbalance, k_P and k_Q can also be used to tune the resynchronization time.

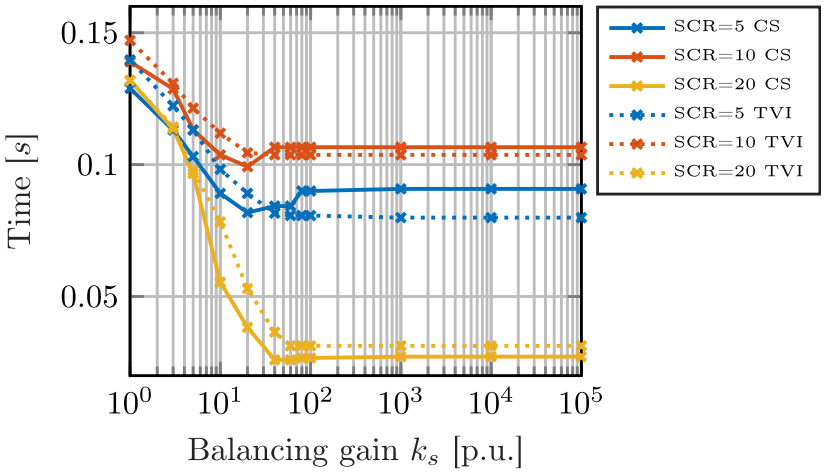

Figure 7.12: Resynchronization time as a function of phase balancing gain $k_s = k_P = k_Q$ for TVI (dotted) and CSA (solid).

7.5 Interactions with system protection

Finally, we investigate interactions of generalized three-phase grid-forming control with distance protection.

7.5.1 Distance protection

In this study, we focus on the distance relay with quadrilateral characteristics. Figure 7.13 illustrates the quadrilateral characteristic of the distance relay. This relay offers the advantage of independently adjustable resistive reach and is recognized for its resilience against the impact of fault resistance [40]. To streamline the relay model, we focus on the digital relay's logic and mechanisms, omitting the inclusion of current and voltage transformers. These transformers typically step down signals to fit within the operational scope of the relays. Moreover, to facilitate our anal-

ysis, a Fourier analysis is used to estimate fundamental voltage and current phasors. Operating based on the estimated voltage and current phasors from the Fourier analysis, the relay computes the line impedance between the circuit breaker and fault points. All three line-to-line impedance and three line-to-ground impedance are calculated by the relay. If any of the calculated impedance values fall within a predefined zone, the relay initiates a trip signal after a defined operating time.

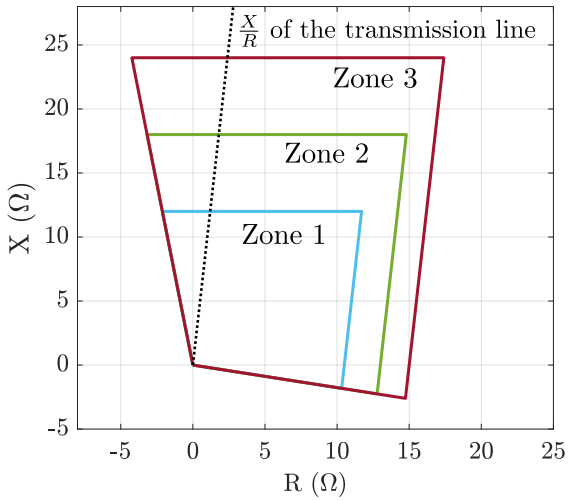

Figure 7.13: Quadrilateral characteristic of the distance relay.

Line-to-line (LL) faults have been recognized as critical scenarios leading to protection failures [26]. Consequently, we have directed our attention towards examining a phase *a* to phase *b* fault as an illustrative case study. It is important to note that the transient stability during fault recovery under LL fault conditions is compromised when using the CSA. This is primarily due to the occurrence of controller windup within the voltage loop. Consequently, in our simulations, the TVI method is used as the current limiting strategy for the GFM converter to enhance the transient stability.

The test system depicted in Figure 7.14 is equipped with four breakers, each paired with a corresponding distance relay ($\mathscr{R}_1$, $\mathscr{R}_2$, $\mathscr{R}_3$, and $\mathscr{R}_4$).

These breakers are placed at both terminals of the 40 km double circuit high voltage transmission

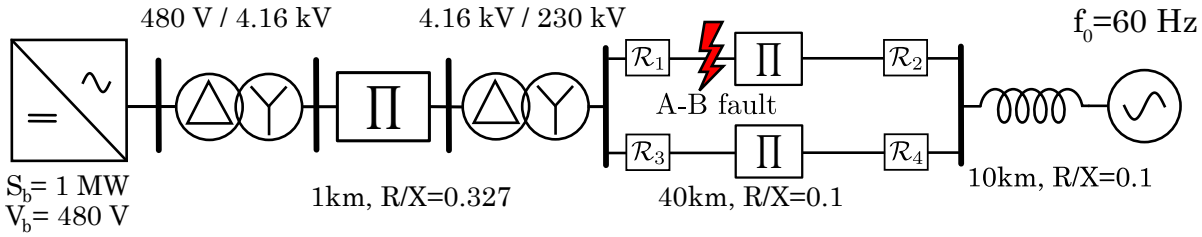

Figure 7.14: Test system with a low-voltage VSC connected to a weak ac system through a distribution line, double circuit transmission line with four distance relays, and step up transformers.

line. A phase a to phase b fault is simulated on the upper transmission line, occurring at a distance $\rho \in (0,1)$ relative to the length of the upper transmission line. Notably, the impedance between the fault location and relay $\mathscr{R}_1$ is given by ρZ_l, while the impedance between the fault location and relay $\mathscr{R}_2$ is $(1-\rho)Z_l$, wherein Z_l represents the impedance of each transmission line.

In the case of a phase a to phase b fault involving a fault resistor, denoted as R_f, relays $\mathscr{R}_1$ and $\mathscr{R}_2$ evaluate the LL loop impedance by

$$Z^{\mathrm{ab}}_{\mathscr{R}_1} = \rho Z_l + R_f \left(1 + \frac{I^{\mathrm{a}}_{\mathscr{R}_2} - I^{\mathrm{b}}_{\mathscr{R}_2}}{I^{\mathrm{a}}_{\mathscr{R}_1} - I^{\mathrm{b}}_{\mathscr{R}_1}}\right), \tag{7.1a}$$

$$Z^{\mathrm{ab}}_{\mathscr{R}_2} = (1-\rho) Z_l + R_f \left(1 + \frac{I^{\mathrm{a}}_{\mathscr{R}_1} - I^{\mathrm{b}}_{\mathscr{R}_1}}{I^{\mathrm{a}}_{\mathscr{R}_2} - I^{\mathrm{b}}_{\mathscr{R}_2}}\right). \tag{7.1b}$$

Here, $I^{\mathrm{a}}_{\mathscr{R}_1}$ ($I^{\mathrm{a}}_{\mathscr{R}_2}$) and $I^{\mathrm{b}}_{\mathscr{R}_1}$ ($I^{\mathrm{b}}_{\mathscr{R}_2}$) represent the complex current phasors of phase a and b received by relay $\mathscr{R}_1$ at the inverter-side (relay $\mathscr{R}_2$ at the grid-side), respectively. It should be noted that the calculated impedance obtained by the relays may differ from the actual fault impedance. Such deviations can arise due to the presence of fault resistance R_f, as well as the differences between the inverter-side and grid-side current phasors. For instance, an additional impedance is factored into the calculation made by relay $\mathscr{R}_1$, and this can be expressed as $R_f \left(\frac{I^{\mathrm{a}}_{\mathscr{R}_2} - I^{\mathrm{b}}_{\mathscr{R}_2}}{I^{\mathrm{a}}_{\mathscr{R}_1} - I^{\mathrm{b}}_{\mathscr{R}_1}}\right)$. This additional impedance is influenced by the value of fault resistance R_f and the ratio between the grid-side and inverter-side current phasor.

Phase a to phase b fault with $R_f = 0.001\ \Omega$

The distance relay parameters are given in Table. 7.3, including the percentage of the transmission line length covered by each zone, the resistive reach of each zone, and the operation time.

Protection zone	Percentage	Resistive reach	Operating time
Zone 1	100 %	10.5 Ω	100 ms
Zone 2	150 %	13 Ω	250 ms
Zone 3	200 %	15 Ω	400 ms

Table 7.3: Distance Relay Parameters.

Figure 7.15 shows the impedance diagram computed by relay $\mathscr{R}_1$ and relay $\mathscr{R}_2$ during a phase a to phase b fault, with fault resistance $R_f = 0.001\ \Omega$. Notably, the measured impedance from both relays closely aligns with the actual fault impedance extending from the relay to the fault location. Given the minimal fault resistance R_f, the additional impedance calculated by the relays becomes negligible, ensuring the proper functionality of both relays for normal tripping operations in this specific scenario.

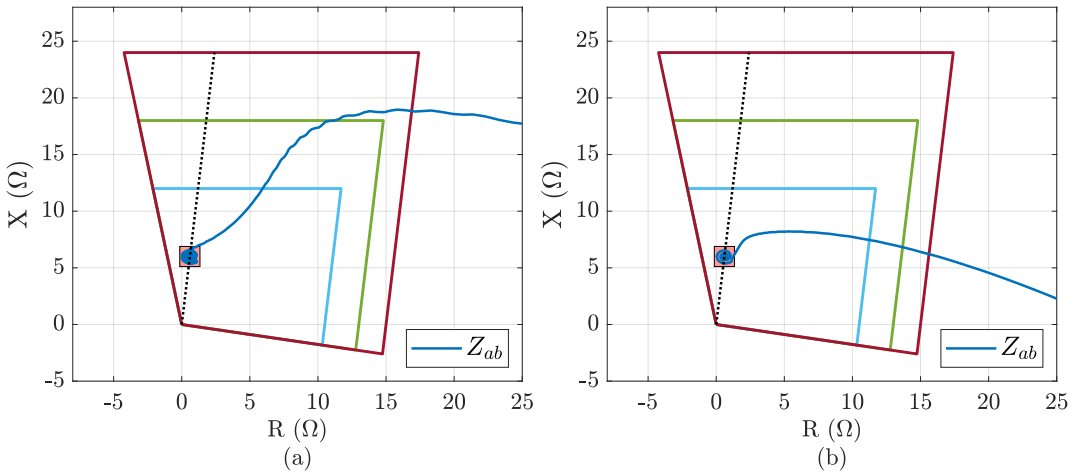

Figure 7.15: Phase a to phase b impedance diagram, Z_{ab}, computed by (a) relay $\mathscr{R}_1$ and (b) relay $\mathscr{R}_2$ during a phase a to phase b fault with $R_f = 0.001\Omega$. The red square represents the actual fault impedance between the respective relay and the fault location.

Phase a to phase b fault with $R_f = 5\ \Omega$

In Figure 7.16, the impedance diagram measured by relay $\mathscr{R}_1$ and relay $\mathscr{R}_2$ are depicted for a phase a to phase b fault with fault resistance $R_f = 5\ \Omega$. Observations in Figure 7.16b reveal that relay $\mathscr{R}_2$ effectively triggers a normal trip due to the close alignment between the impedance measurement and the actual impedance. However, the impedance measured by relay $\mathscr{R}_1$ deviates from the actual impedance and leads to a misoperation, as presented in Figure 7.16a. It is revealed that the additional impedance calculated by relay $\mathscr{R}_1$ manifests as resistive, quantified as 15Ω. Consequently, in compliance with (7.1a), the computed ratio $\frac{I^{\mathrm{a}}_{\mathscr{R}_2} - I^{\mathrm{b}}_{\mathscr{R}_2}}{I^{\mathrm{a}}_{\mathscr{R}_1} - I^{\mathrm{b}}_{\mathscr{R}_1}}$ yields a value of 3.

Considering the distribution line and high voltage transformer, the electrical distance from the fault location to the grid is significantly shorter in comparison to the distance to the GFM converter. Furthermore, the output current of the GFM converter is limited by its current limiting strategy (i.e., TVI). As a result, the contribution of the fault current from the converter becomes inconsequential when compared to the fault current originating from the grid. In this context, the fault current feeding into both relay $\mathscr{R}_1$ and relay $\mathscr{R}_2$ predominantly arises from the grid under a short-circuit fault in the double circuit transmission line. The fault current from the grid comprises two components. The first component flows directly from the grid through relay $\mathscr{R}_2$ to the fault location. The second component follows a route through relay $\mathscr{R}_4$, relay $\mathscr{R}_3$, and finally relay $\mathscr{R}_1$ before reaching the fault position. Both components have the same phase. Consequently, the ratio of the current flowing through relay $\mathscr{R}_2$ to relay $\mathscr{R}_1$ becomes linked to the line impedance along this particular route, equating to $\frac{1+\rho}{1-\rho} = 3$ when the fault position coincides with the midpoint of transmission line 1 (i.e., $\rho = 0.5$). Furthermore, the additional impedance calculated by relay $\mathscr{R}_2$ is also resistive, specifically measuring $R_f \left(\frac{1-\rho}{1+\rho}\right) = \frac{5}{3}\ \Omega$. As depicted in Figure 7.16b, the simulation results align with this analysis.

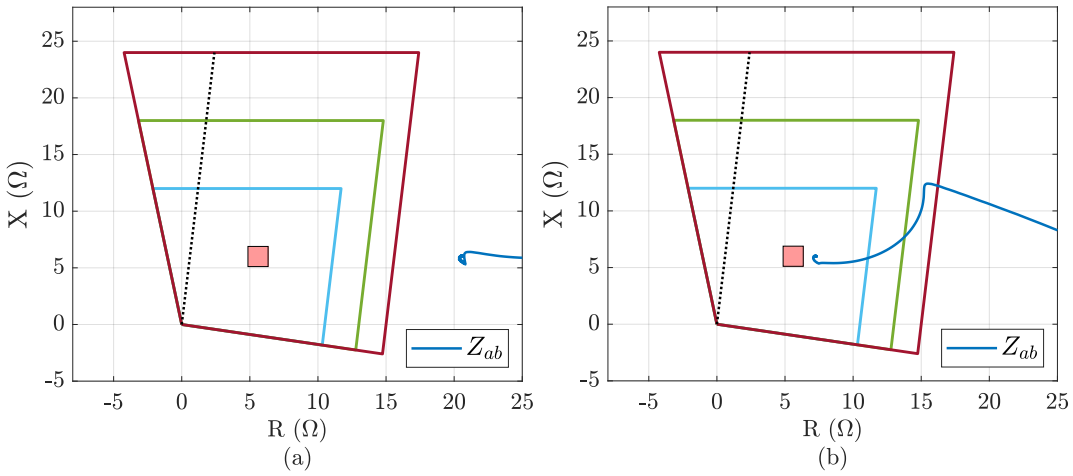

Figure 7.16: Phase a to phase b impedance diagram, Z_{ab}, computed by (a) relay $\mathscr{R}_1$ and (b) relay $\mathscr{R}_2$ during a phase a to phase b fault with $R_f = 5\Omega$. The red square represents the actual fault impedance between the respective relay and the fault location.

An important consideration is that, following the tripping action by relay $\mathscr{R}_2$, the configuration of the double circuit transmission line system changes to a single-ended network. As a result, relay $\mathscr{R}_1$ can precisely compute the impedance value, enabling it to initiate normal tripping operations. This observation underscores the adaptability and reliability of the protection scheme. Overall, it is imperative to closely pay attention to the interactions between GFM converters and transmission system-level protection, particularly in future power systems with high penetration of inverter-based resources. The fault current of the converter is restricted due to inherent limitations in the current capacity. Additionally, the current response of the GFM converter is entirely contingent on its control system, a characteristic that sharply contrasts with the behavior of synchronous generators.

8. Case study: distribution

This chapter describes a distribution system benchmark system based on the IEEE 13-bus feeder that was developed in this project to illustrate and verify the unbalanced fault ride through capabilities of the controls developed in this project. The system is used to study the impact of current limiting strategies on the response of a grid-forming converter in a distribution system with inverse time overcurrent relays and induction motor loads. Moreover, the system is used to illustrate the unbalanced cold start method described in Chapter 6.

8.1 Benchmark system

The benchmark system is shown in Figure 8.1 and uses the network data of the IEEE 13-bus feeder. Inverse time overcurrent relays, a grid-forming converter, and an induction motor load have been integrated into the system.

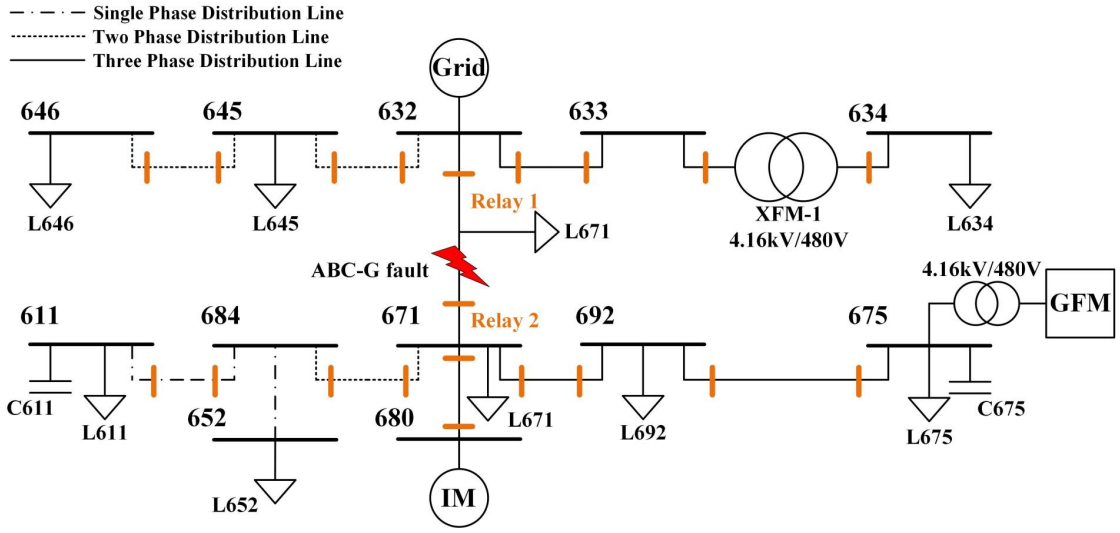

Figure 8.1: IEEE 13 bus distribution system with GFM converter, induction motor load, and inverse time relay (indicated in orange).

8.2 Overcurrent protection

We first study the impact of the grid-forming converter on overcurrent protection during a symmetric fault between Relay 1 and Relay 2 (see Figure 8.1).

8.2.1 Inverse time overcurrent relay

The inverse time overcurrent relay is modeled in this study, which comprises two protection units: a phase protection unit and an earth protection unit. The phase protection unit is activated when the current value in any of the phases surpasses the predetermined pickup value. Similarly, the

earth protection unit is activated when the value of the zero-sequence current exceeds the specified pickup value. Upon activation of either protection unit lasting for the relay operating time, a trip signal is generated and transmitted to the breaker.

The relay operating time is contingent upon the pickup value (I_{pickup}) and the time multiplier setting (t_{TMS}) of the relay. The relay operating time is calculated based on the IEEE standard [41], expressed as

$$t_{op} = t_{TMS}\left(\frac{A}{M^p} + B\right). \tag{8.1}$$

Here, M represents the current expressed in multiples of pickup current ($I_{\text{input}}/I_{\text{pickup}}$), while A, B, p are constants selected to shape the desired curve characteristics. These constants are detailed in Table. 8.1 [41].

Characteristic	A	B	p
Moderately inverse	0.0515	0.1140	0.0200

Table 8.1: Constants for standard characteristics of the inverse time overcurrent relay.

8.2.2 Response to a symmetric ground fault

To investigate on the GFM converter performance on the existing protection relays, a symmetric ground fault is simulated between Relay 1 and Relay 2. For our initial simulation, the settings of Relay 1 and Relay 2 have been tuned based on the expected fault current contribution flowing from the grid (modeled as infinite bus) to the fault, i.e., disregarding the GFM converter. This simulation illustrates the implications for the fault response of the system when connecting a GFM converter without updating the protection settings.

In this scenario, Relay 1 trips due to the fault current provided by from the bulk grid (modeled as infinite bus). However, due to the limited GFM converter fault current Relay 2 does not trip, the lower half of the system remains energized by the GFM converter, and the fault is not cleared. The currents across the relay are shown in Figure 8.2a and Figure 8.2b, respectively. We emphasize that the black dotted line indicates the trip limit of the relays and the blue and the pink dotted lines indicate the magnitude of the current at which the relay trips after the time specified in the figure. Notably, as the current magnitude increases the time taken for the relay to trip also reduces depicting the inverse time relay characteristics.

Next we investigate two broad approaches to avoid misoperation of the protection system. First we investigate lowering the thresholds of Relay 1 and Relay 2. An alternative solution is to increase the current rating of the GFM converter.

To avoid the GFM converter feeding into the fault, the settings of Relay 1 and Relay 2 settings are changed to 70% of their original rating to enforce tripping at lower current that is within the current capability of the GFM converter. After this change, both relays trip as shown in Figure 8.2c and

Figure 8.2b. We emphasize that lowering the threshold further would risk tripping the protection during startup of the induction motor load.

Finally, if the relay settings are kept at their original settings, the GFM converter current limit has to be increase by 40 % to reliably trip Relay 1 and Relay 2 as shown in Figure 8.2e and Figure 8.2f, respectively.

This result, highlights the need to investigate existing infrastructure and protection settings before including the GFM converters into distribution systems in large numbers. In principle, lowering the relay thresholds may be seen as a more economic alternative to oversizing the GFM converter to increase its fault current capabilities. However, this option may not always be viable and the expected inrush current of loads (e.g., induction machines) and transformers has to be well below the thresholds of the protection system to avoid misoperation. Thus, if the system is already significantly loaded, increasing the fault current capabilities of the GFM converter may be the only viable options.

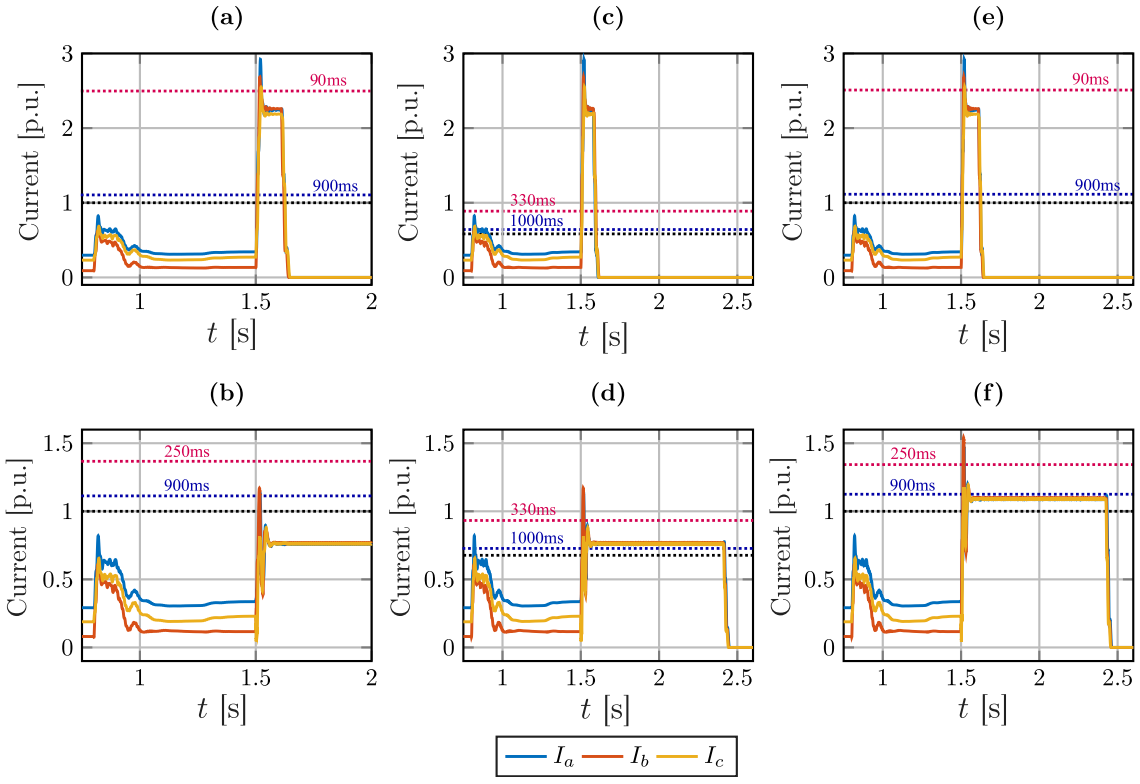

Figure 8.2: Symmetric short circuit fault with inverse time relay. The subplots (a), (c), and (e) indicate the response of Relay 1 while the subplots (b), (d), and (f) indicate the response of Relay 2.

8.3 Cold start of IEEE 13-bus system

Finally, the effectiveness of the generalized three-phase droop control and the impact of the phase balancing gain $k_P = k_Q = k_s$ and distributed cold start methods presented in Chapter 6 are investigated through the restoration of the unbalanced IEEE 13-bus system from a complete blackout.

The system configuration and parameters are shown in Figure 8.3. Two GFM converters with different phase balancing gains are connected to the distribution system, and multiple breakers with load relays in the system are marked in blue color. The simulation results depicted in Figure 8.4, demonstrate the cold start capability of GFM converters for different phase balancing gains k_s and the gradual connection/energization of loads as controlled by the advanced load relays.

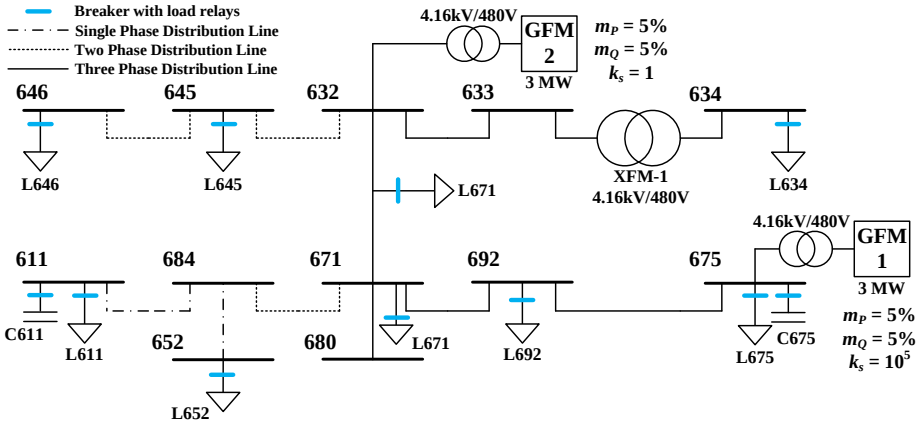

Figure 8.3: IEEE 13-bus distribution system with two GFM converters and breakers with load relays (indicated in blue) responses

GFM converter 1 initiates a soft start at $t = 3$ s with $k_s = 10^5$, and current limiting mitigating inrush currents. In contrast, GFM converter 2 synchronizes and connects to the system at $t = 5$ s and uses $k_s = 1$. The unbalance factors for the terminal voltage and power of the two converters after completing the system restoration are compared in Table. 8.2.

The results of Figure 8.4(c) and (d) and Table. 8.2 reveal that GFM converter 1 exhibits balanced steady-state phase voltages but imbalanced active power dispatch across the three phases. In con-

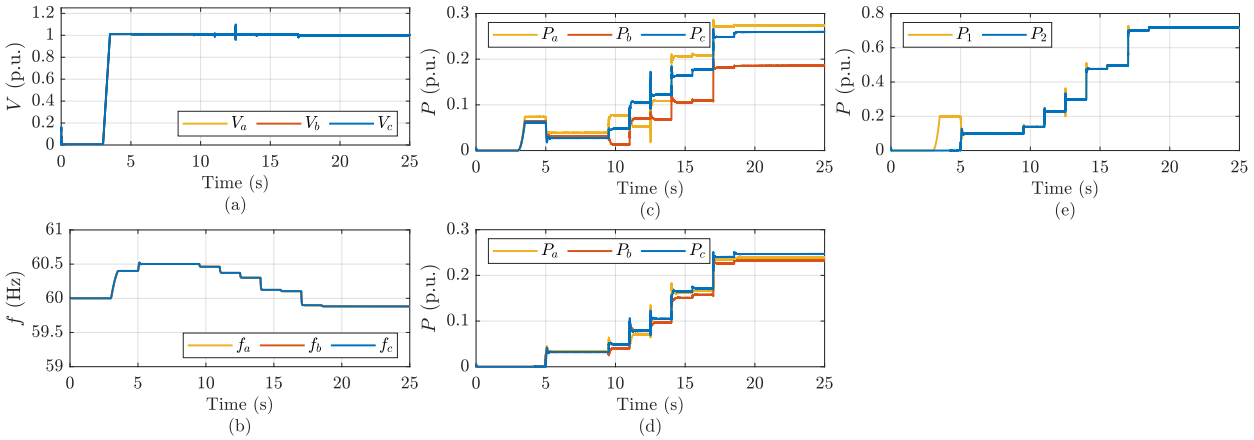

Figure 8.4: Simulation results for the cold start of the IEEE 13-bus system. Voltage magnitude (a) and frequency (b) for each phase of GFM converter 1. Active power for each phase of GFM converter 1 (c) and GFM converter 2 (d). Total active power of GFM converter 1 and GFM converter 2 (e).

trast, GFM converter 2 demonstrates a significantly improved balance in active power but exhibits imbalanced phase voltages. Despite exhibiting imbalanced phase voltages or active power, the total active power is accurately shared between the two GFM converters as shown in Figure 8.4(e), emphasizing the ability of the generalized three-phase droop control to adjust the sharing of load unbalance through the phase balancing gain $k_P = k_Q = k_s$ while addressing voltage and power imbalances during cold start operations.

Description	GFM 1	GFM 2
Voltage unbalance factor	0.08 %	2.58 %
Active power unbalance factor	5.40 %	0.74 %

Table 8.2: Steady-state unbalance factors in %.

9. Conclusion

This project developed a generalized three-phase grid-forming control that can control phase voltage with reliable unbalanced fault ride through capabilities. The generalized three-phase grid-forming control applies grid-forming control and current limiting separately to every phase. In addition, a phase-balancing feedback is developed to synchronize the controls of every phase and adjust trade-offs between voltage unbalance, power unbalance as well as the sharing of unbalanced load by multiple converters. In this context, two common current limiting methods for grid-forming control have been extended to enable unbalanced fault ride through and a novel hybrid threshold virtual impedance current limiting method has been developed that can effectively limit the converter current under large phase angle jumps. Finally, we developed an initial method for distributed cold-start methods for unbalanced distribution feeders that do not require centralized coordination and leverage the capabilities of distribution connected grid-forming converters and advanced load relays. Instead of energizing an entire distribution feeder at once, this approach relies on autonomously sequencing the energization of loads at a more granular level during a cold-start process initiated by grid-forming converters.

The effectiveness of the control algorithms developed in this project and study the interactions of grid-forming converters with the system protection, we developed two benchmark systems modeling (i) a segment of a system consisting of a medium voltage feeder and a high voltage double circuit transmission line used to study transmission faults and interactions of the converter control and protection with distance relays, and (ii) a distribution system benchmark based on the IEEE 13-bus feeder used to study the impact of unbalanced loads interactions of grid-forming converters with line overcurrent protection.

Interesting topics for future work include more detailed investigations of transient stability during faults and after fault clearing as well as more in depth investigations of protection system settings in converter-dominated systems. Moreover, further research is needed to evaluate the performance and implementation of decentralized cold start methods for distribution feeders with significant shares of grid-forming converters.

Finally, while the current limiting methods developed in this project enable a significantly improved response to unbalanced faults, the topic of current limiting remains the subject of much debate. In particular, the vast majority of current limiting methods are based on heuristic for specific cases to some extent. As a result, their response to corner cases can be hard to predict. In this context, the biggest challenge appears to be that to date no technology-agnostic functional requirements for fault ride through of grid-forming converters exist that can inform the design and, ultimately, standardization of current limiting controls and fault ride through strategies.

References

[1] M. Chandorkar, D. Divan, and R. Adapa, "Control of parallel connected inverters in standalone ac supply systems," *IEEE Trans. Ind. Appl.*, vol. 29, no. 1, pp. 136–143, 1993.

[2] S. D'Arco, J. A. Suul, and O. B. Fosso, "A virtual synchronous machine implementation for distributed control of power converters in smartgrids," *Electr. Power Sys. Res.*, vol. 122, pp. 180–197, 2015.

[3] R. J. Campbell, "Weather-related power outages and electric system resiliency," Congressional Research Service, Tech. Rep., 2012.

[4] "1200 mw fault induced solar photovoltaic resource interruption disturbance report," NERC, Tech. Rep., 2017.

[5] "Black system south australia 28 september 2016," AEMO, Tech. Rep., 2017.

[6] "Queensland and south australia system separation on 25 august 2018," AEMO, Tech. Rep., 2019.

[7] A. Crivellaro, A. Tayyebi, C. Gavriluta, D. Groß, A. Anta, F. Kupzog, and F. Dörfler, "Beyond low-inertia systems: Massive integration of grid-forming power converters in transmission grids," in *IEEE Power & Energy Society General Meeting*, 2020.

[8] "Impact of inverter based generation on bulk power system dynamics and short-circuit performance," IEEE/NERC Task Force, Tech. Rep., 2018.

[9] J. Jia, G. Yang, A. H. Nielsen, and P. Rønne-Hansen, "Impact of VSC control strategies and incorporation of synchronous condensers on distance protection under unbalanced faults," *IEEE Trans. Ind. Electron.*, vol. 66, no. 2, pp. 1108–1118, 2019.

[10] IEEE Power System Relaying Committee Working Group, "Single phase tripping and auto reclosing of transmission lines," *IEEE Trans. Power Del.*, vol. 7, no. 1, pp. 182–192, 1992.

[11] J. Rocabert, A. Luna, F. Blaabjerg, and P. Rodríguez, "Control of power converters in ac microgrids," *IEEE Trans. Power Electron.*, vol. 27, no. 11, pp. 4734–4749, 2012.

[12] J. Matevosyan, B. Badrzadeh, T. Prevost, E. Quitmann, D. Ramasubramanian, H. Urdal, S. Achilles, J. MacDowell, S. H. Huang, V. Vital, J. O'Sullivan, and R. Quint, "Grid-forming inverters: Are they the key for high renewable penetration?" *IEEE Power and Energy Magazine*, vol. 17, no. 6, pp. 89–98, 2019.

[13] M. C. Chandorkar, D. M. Divan, and R. Adapa, "Control of parallel connected inverters in standalone AC supply systems," *IEEE Trans. Ind. Appl.*, vol. 29, no. 1, pp. 136–143, 1993.

[14] S. D'Arco, J. A. Suul, and O. B. Fosso, "A virtual synchronous machine implementation for distributed control of power converters in smartgrids," *Electr. Power Sys. Res.*, vol. 122, pp. 180–197, 2015.

[15] T. Qoria, F. Gruson, F. Colas, X. Kestelyn, and X. Guillaud, "Current limiting algorithms and transient stability analysis of grid-forming VSCs," *Electr. Power Sys. Res.*, vol. 189, p. 106726, 2020.

[16] B. Kroposki, B. Johnson, Y. Zhang, V. Gevorgian, P. Denholm, B.-M. Hodge, and B. Hannegan, "Achieving a 100% renewable grid: Operating electric power systems with extremely

high levels of variable renewable energy," *IEEE Power Energy Mag.*, vol. 15, no. 2, pp. 61–73, 2017.

[17] E. Nasr-Azadani, C. A. Cañizares, D. E. Olivares, and K. Bhattacharya, "Stability analysis of unbalanced distribution systems with synchronous machine and dfig based distributed generators," *IEEE Trans. Smart Grid*, vol. 5, no. 5, pp. 2326–2338, 2014.

[18] J. Jia, G. Yang, and A. H. Nielsen, "A review on grid-connected converter control for short-circuit power provision under grid unbalanced faults," *IEEE Trans. Power Del.*, vol. 33, no. 2, pp. 649–661, 2018.

[19] A. D. Paquette and D. M. Divan, "Virtual impedance current limiting for inverters in microgrids with synchronous generators," *IEEE Trans. Ind. Appl.*, vol. 51, no. 2, pp. 1630–1638, 2015.

[20] Q. Taoufik, H. Wu, X. Wang, and I. Colak, "Variable virtual impedance-based overcurrent protection for grid-forming inverters: Small-signal, large-signal analysis and improvement," *IEEE Trans. Smart Grid*, 2022.

[21] D. Groß and F. Dörfler, "Projected grid-forming control for current-limiting of power converters," in *Allerton Conference on Communication, Control, and Computing*, 2019, pp. 326–333.

[22] E. Avdiaj, J. A. Suul, S. D'Arco, and L. Piegari, "A virtual synchronous machine-based control for eliminating DC-side power oscillations of three-phase VSCs under unbalanced grid voltages," in *Int. Conference on Compatibility, Power Electronics and Power Engineering*, 2021.

[23] M. A. Awal, M. R. K. Rachi, H. Yu, I. Husain, and S. Lukic, "Double synchronous unified virtual oscillator control for asymmetrical fault ride-through in grid-forming voltage source converters," *IEEE Trans. Power Electron.*, 2022.

[24] N. Baeckeland, D. Venkatramanan, M. Kleemann, and S. Dhople, "Stationary-frame grid-forming inverter control architectures for unbalanced fault-current limiting," *IEEE Trans. Energy Convers.*, vol. 37, no. 4, pp. 2813–2825, 2022.

[25] D. Groß, M. Colombino, B. Jean-Sébastien, and F. Dörfler, "The effect of transmission-line dynamics on grid-forming dispatchable virtual oscillator control," *IEEE Trans. Control Netw. Syst.*, vol. 6, no. 3, pp. 1148–1160, 2019.

[26] N. Baeckeland, D. Venkatramanan, S. Dhople, and M. Kleemann, "On the distance protection of power grids dominated by grid-forming inverters," in *IEEE PES Innovative Smart Grid Technologies Conference Europe (ISGT-Europe)*, 2022, pp. 1–6.

[27] Y. Du, H. Tu, X. Lu, J. Wang, and S. Lukic, "Black-start and service restoration in resilient distribution systems with dynamic microgrids," *IEEE Trans. Emerg. Sel. Topics Power Electron.*, vol. 10, no. 4, pp. 3975–3986, 2022.

[28] M. Mirzadeh, R. Strunk, S. Matter, I. Bekker, M. Munderloh, T. Erckrath, L. Hofmann, and A. Mertens, "A rule-based concept for a bottom-up multi-master black start of an inverter-dominated low-voltage cell," in *IEEE International Symposium on Power Electronics for Distributed Generation Systems (PEDG)*, 2022, pp. 1–6.

[29] T. Kim, S. Santoso, V. C. Cunha, W. Wang, R. Dugan, D. Ramasubramanian, and A. Maitra, "Blackstart of unbalanced microgrids using grid-forming inverter with voltage balancing capability," in *IEEE PES Transmission and Distribution Conference and Exposition (T&D)*, 2022, pp. 1–5.

[30] R. V. Ferreira, S. M. Silva, and D. I. Brandao, "Positive–negative sequence synchronverter for unbalanced voltage in ac grids," *Journal of Control, Automation and Electrical Systems*, vol. 32, no. 3, pp. 711–720, 2021.

[31] T. Qoria, F. Gruson, F. Colas, X. Guillaud, M.-S. Debry, and T. Prevost, "Tuning of cascaded controllers for robust grid-forming voltage source converter," in *Power Systems Computation Conference*, 2018.

[32] D. Groß, M. Colombino, J.-S. Brouillon, and F. Dörfler, "The effect of transmission-line dynamics on grid-forming dispatchable virtual oscillator control," *IEEE Trans. Control Netw. Syst.*, vol. 6, no. 3, pp. 1148–1160, 2019.

[33] T. Qoria, F. Gruson, F. Colas, G. Denis, T. Prevost, and X. Guillaud, "Critical clearing time determination and enhancement of grid-forming converters embedding virtual impedance as current limitation algorithm," *IEEE Trans. Emerg. Sel. Topics Power Electron.*, vol. 8, no. 2, pp. 1050–1061, 2020.

[34] B. Fan, T. Liu, F. Zhao, H. Wu, and X. Wang, "A review of current-limiting control of grid-forming inverters under symmetrical disturbances," *IEEE Open Journal of Power Electronics*, vol. 3, pp. 955–969, 2022.

[35] R. Rosso, S. Engelken, and M. Liserre, "On the implementation of an FRT strategy for grid-forming converters under symmetrical and asymmetrical grid faults," *IEEE Trans. Ind. Appl.*, vol. 57, no. 5, pp. 4385–4397, 2021.

[36] S. S. Nudehi and D. Groß, "Grid-forming control of three-phase and single-phase converters across unbalanced transmission and distribution systems," *IEEE Trans. Power Syst.*, 2022, early access.

[37] T. Gönen, *Electric power distribution system engineering*. CRC press Boca Raton, FL, USA, 2008, vol. 2.

[38] C. Wang, A. Bernstein, J.-Y. Le Boudec, and M. Paolone, "Existence and uniqueness of load-flow solutions in three-phase distribution networks," *IEEE Trans. Power Syst.*, vol. 32, no. 4, pp. 3319–3320, 2017.

[39] M. Lu, S. Dhople, D. Zimmanck, and B. Johnson, "Spontaneous phase balancing in delta-connected single-phase droop-controlled inverters," *IEEE Trans. Power Electron.*, 2022.

[40] A. Hooshyar, M. A. Azzouz, and E. F. El-Saadany, "Distance protection of lines emanating from full-scale converter-interfaced renewable energy power plants—part i: Problem statement," *IEEE Transactions on Power Delivery*, vol. 30, no. 4, pp. 1770–1780, 2015.

[41] "IEEE standard for inverse-time characteristics equations for overcurrent relays," *IEEE Std C37.112-2018 (Revision of IEEE Std C37.112-1996)*, pp. 1–25, 2019.